https://doi.org/10.5194/egusphere-2026-1476
Preprint. Discussion started: 18 June 2026

Assessing Cloud Representation in Two Microphysics Schemes of MPAS-Atmosphere Model (version 8.2.2) over the Maritime Continent with Himawari-9 AHI Observations

Xuewei Zhang,[1,3] Lipeng Jiang,[1,4] Zhiquan Liu[1], Tao Sun[2], Wei Wang[1], I-Han Chen[2]

[1]NSF National Center for Atmospheric Research, Boulder, Colorado, USA
[2]Centre for Climate Research Singapore, Singapore
[3]Key Laboratory of Meteorological Disaster, Ministry of Education (KLME)/Joint International Research Laboratory of Climate and Environment Change (ILCEC)/Collaborative Innovation Center on Forecast and Evaluation of Meteorological Disasters (CIC-FEMD), Nanjing University of Information Science & Technology, Nanjing, China
[4]Earth System Modeling and Prediction Center, China Meteorological Administration, Beijing, China

Correspondence to: Xuewei Zhang (xwzhang@nuist.edu.cn)

Abstract. Tropical cloud prediction over the Maritime Continent remains challenging for numerical weather prediction models, largely due to uncertainties in cloud microphysics parameterizations under complex topography and multiscale convective conditions. Accurate cloud forecasts are essential for assimilating cloud-affected observations, particularly high-resolution radiances from geostationary satellites, which also provide a valuable basis for diagnosing model performance of clouds. In this study, tropical cloud characteristics simulated by the Model for Prediction Across Scales–Atmosphere (MPAS-A) with two cloud microphysics schemes—the single-moment WSM6 and the double-moment NSSL, are comprehensively evaluated using multi-band radiances from the Himawari-9 Advanced Himawari Imager (AHI) and associated Level-2 cloud products. The proposed infrared radiance–based framework enables more effective use of high-resolution satellite data for model assessment. Results indicate that NSSL better captures the spatial distribution of cloud amount and yields smaller forecast-minus-observation (F–O) brightness temperature biases in cloud- and fog-sensitive channels. In contrast, WSM6 shows smaller F–O biases in water-vapor-sensitive channels, but reduced skill in distinguishing cloudy and clear-sky conditions during the spin-up period. Cloud-type diagnostics further reveal that WSM6 and NSSL tend to underpredict the occurrence of thick and thin ice clouds, respectively. Nevertheless, both schemes show higher forecast skills for liquid-water and thin ice clouds than for other cloud types, whereas the largest forecast errors occur in multilayer ice-cloud regimes. An overprediction of cloud-top heights for high-level clouds is also evident in both schemes, with diurnal variations in F–O that are more pronounced over land in the NSSL scheme.

https://doi.org/10.5194/egusphere-2026-1476
Preprint. Discussion started: 18 June 2026

1 Introduction

Cloud prediction in the tropics has long posed a major scientific and operational challenge due to the deep convection, complex multiscale interactions, sparse in situ observations, and strong ocean–atmosphere–radiation coupling that remain difficult for numerical models to represent (Jin et al., 2018; Medeiros et al., 2021; Gehne et al., 2022; Stephens et al., 2024). Within the tropical belt (~10° N–10° S, 90°–150° E), the Maritime Continent is characterized by exceptional complexity, with numerous islands, shallow seas, and rugged mountainous terrain that further complicate weather prediction (Neale and Slingo, 2003; Chang et al., 2016; Dipankar et al., 2020; Aslam, 2025). Despite the deployment of convection-permitting models with increasingly high spatial resolution, the accurate representation of cloud microphysical processes in this region remains unresolved, and forecast skill continues to be constrained by uncertainties in microphysics parameterizations under such complex boundary and atmospheric conditions (Khain et al., 2015; Chow et al., 2016; Simón-Moral et al., 2021; Lee et al., 2022).

In numerical weather prediction (NWP) systems, microphysical parameterizations play a fundamental role in regulating cloud simulations by governing hydrometeor classification, interactions between species, latent heat release, and radiative properties, all of which form a complex microphysical–dynamical–radiative coupling mechanism (Fovell et al., 2010; Zhang et al., 2021; Morrison et al., 2020; Köcher et al., 2023; Atlas et al., 2024). Commonly used schemes are broadly categorized into single-moment and double-moment approaches, whose different representations of hydrometeor mass and number concentration lead to distinct particle size distributions, sedimentation characteristics, and phase partitioning. Each cloud microphysics scheme relies on specific assumptions regarding cloud and precipitation hydrometeor properties, which can be a significant source of model error (Tong and Xue, 2008). Moreover, the effectiveness of assimilating cloud-affected satellite observations is strongly influenced by the representation of cloud microphysics (Sieron et al., 2017; Rendon et al., 2025). For example, inter-scheme differences in the treatment of latent cooling within the background state vector and associated error covariance matrices may affect data assimilation performance (Wheatley et al., 2014). Differences in hydrometeor fall velocities likewise alter background brightness temperatures (BTs) in data assimilation, as faster sedimentation transports hydrometeors from cloud tops to lower altitudes, resulting in higher simulated BTs (van Weverberg et al., 2013; Jones et al., 2018; Griffin and Otkin, 2022). In addition, simulated BTs are highly sensitive to the hydrometeor profiles provided to the radiative transfer model (Wang, Chipilski, et al., 2020; Wang, Su, et al., 2020; Li et al., 2022). Consequently, systematic assessment and refinement of cloud microphysics parameterization schemes remain a key prerequisite for improving model cloud predictability.

Given the sparsity of in situ observations and the limited spatial coverage of ground-based measurements in the tropics, satellite observations have become an indispensable basis for evaluating cloud parameterization schemes (Jones et al., 2013; Centurioni et al., 2019; Battaglia et al., 2020). Among these, microwave radiances provide valuable information on the vertical structure of hydrometeors (Matsui et al., 2014; Panegrossi et al., 2016; Galligani et al., 2017; Zhang et al., 2019). However, their relatively coarse temporal sampling, constrained by sun-synchronous orbits, limits their ability to continuously capture

https://doi.org/10.5194/egusphere-2026-1476
Preprint. Discussion started: 18 June 2026

the diurnal variability of clouds (Wang and Zhao, 2017). In contrast, geostationary infrared (IR) observations offer high-frequency, spatially continuous coverage over broad regions, enabling detailed monitoring of cloud systems and their diurnal evolution (Bessho et al., 2016; Schmit et al., 2017; Aumann et al., 2018; Susskind et al., 2019; Min et al., 2020).

Two general approaches are commonly used to assess cloud microphysics parameterization schemes with satellite observations. The first approach is based on direct comparisons between model-simulated hydrometeors and their satellite-retrieved counterparts (Waliser et al., 2009; Huang et al., 2019). This strategy typically relies on interpretable retrieval-based quantities, such as cloud fraction, cloud optical depth, and cloud-top height (CTH), derived from well-established retrieval algorithms (Otkin and Greenwald, 2008; Hashino et al., 2013; Wang et al., 2022; Mohan et al., 2024). These quantities either correspond directly to model prognostic variables or maintain strong physical relationships with them. For example, cloud-property products retrieved from visible and infrared satellite radiances have been widely used to diagnose systematic errors in the simulation of cloud fields (Franklin et al., 2013; Iwabuchi et al., 2016; Geiss et al., 2021; Guo et al., 2024). Using Geostationary Operational Environmental Satellite-9 (GOES-9) cloud-property products, Van Weverberg et al. (2013) further demonstrated that simulations of mesoscale convective systems over the tropical western Pacific are highly sensitive to microphysical parameterizations, particularly to the fall velocity of frozen condensate, which is closely related to particle size distributions.

The second approach employs a model-to-satellite framework, in which atmospheric fields from model output (e.g., temperature, water vapor, and cloud mixing ratios) are converted into simulated radiances or BTs via a forward radiative transfer model, enabling direct comparison with satellite observations (Cintineo et al., 2014; Zhang et al., 2019). This approach mitigates uncertainties associated with retrieval assumptions and provides a physically consistent linkage between model-simulated atmospheric states and satellite-observed radiances. As a result, the model-to-satellite strategy has been widely adopted for evaluating the realism of weather and climate model simulations (Otkin et al., 2009, 2017; Grasso et al., 2014; Yao et al., 2018). For instance, several studies have simulated geostationary imager infrared radiances to examine cloud coverage, diurnal variability, and cloud-property characteristics during high-impact convective events (Line et al., 2016; Griffin et al., 2017a, b; Lindsey et al., 2018). Using GOES channel-4 infrared observations, Thompson et al. (2016) highlighted that realistic representation of ice-cloud radiation properties requires explicit coupling between cloud microphysics and radiative parameterizations. The diurnal and semidiurnal variability of southeastern Pacific stratocumulus clouds was quantitatively evaluated by Painemal et al. (2013) using GOES-10 geostationary observations, revealing increases in cloud-top height and cloud fraction during the early morning followed by afternoon decreases, as well as more complex semidiurnal oscillations in coastal clouds compared to offshore clouds. Furthermore, pronounced diurnal variability in high-level clouds over tropical land was identified through a joint analysis of AIRS and IASI infrared observations, with cloud-type-dependent phase and amplitude signals indicative of strong convective coupling (Feofilov et al., 2019). Growing attention has also been directed toward assessing cloud microphysics schemes within this model-to-satellite evaluation framework. By mapping clear- and cloudy-sky model states into GOES-13 BT space, Jones et al. (2018) demonstrated that convective precipitation within the Warn-on-Forecast System (WoFS) was more realistically represented by the NSSL double-moment microphysics scheme,

https://doi.org/10.5194/egusphere-2026-1476
Preprint. Discussion started: 18 June 2026

although cirrus coverage was substantially overestimated, whereas the Thompson scheme produced more accurate cloud fields overall. Similarly, model-to-satellite analyses based on GOES-13 infrared (10.7 μm) BTs indicate that the WRF single-moment six-class (WSM6) scheme tends to underestimate upper-level ice clouds, with observed anvils suggesting excessive conversion of cloud water to graupel (Grasso et al., 2014). When evaluating simulations against GOES-16 all-sky infrared radiances, Kim et al. (2024) further found that differences in simulated BTs were primarily affected by ice and snow fall velocities, with the NSSL and Morrison schemes producing lower BTs due to slower fall speeds, while the faster-falling ice in the WDM6 scheme resulted in higher BT values. Collectively, these studies highlight the strong diagnostic value of satellite-based verification for improving the representation of cloud microphysical processes in numerical models.

As one of the most advanced geostationary infrared imagers, the Advanced Himawari Imager (AHI) aboard Himawari-8/9 provides high spatiotemporal resolution observations across visible, shortwave-infrared, and thermal-infrared bands, enabling the retrieval of key cloud properties such as optical thickness, cloud type, and cloud-top temperature (Letu et al., 2019). Cloud properties retrieved from Himawari-8 AHI have demonstrated strong consistency with observations from MODIS, CloudSat, CALIPSO, and radiosondes, thereby confirming the reliability of AHI data for cloud evaluation (Liu et al., 2020). Furthermore, cross-comparisons between Himawari-8 and Himawari-9 AHI infrared observations demonstrate high inter-sensor consistency, with root-mean-square errors (RMSEs) below 1.7 K, comparable scan-angle characteristics, and only minor differences relative to RTTOV simulations for channels 7, 9, and 16 (Zhu et al., 2023). Collectively, these studies highlight the strong potential of AHI observations for evaluating model cloud microphysics in tropical regions.

Despite the aforementioned advances, the evaluation and understanding of cloud predictability associated with microphysics parameterization schemes over the Maritime Continent remain relatively limited. Moreover, previous studies have largely focused on either single infrared channels or cloud-retrieved products, which has limited the scope of model evaluation using geostationary infrared satellite observations. In this study, multi-band infrared radiances from the Himawari-9 Advanced Himawari Imager (AHI), together with corresponding Level-2 cloud products, are used to evaluate the performance of two microphysics schemes implemented in the Model for Prediction Across Scales–Atmosphere (MPAS-A) (Skamarock et al., 2012, 2018) in representing tropical cloud systems from multiple perspectives, including BT simulations, cloud amount, cloud-top height, cloud type, and diurnal variability. This synergistic approach is expected to enhance the effective use of satellite observations and to provide a more comprehensive characterization of cloud properties for model evaluation. The primary objective of this study is to offer valuable insights into improving tropical cloud forecasts within a high-resolution regional modelling framework and to lay the groundwork for future assimilation of cloud-affected infrared radiances over this region. The remainder of this paper is organized as follows. Section 2 introduces the datasets, methodology, and model configurations. The results are presented and discussed in Section 3, and Section 4 summarizes the main findings and outlines directions for future prospects.

https://doi.org/10.5194/egusphere-2026-1476
Preprint. Discussion started: 18 June 2026

2 Data, Methodology and Model Settings

2.1 Regional MPAS-Atmosphere model

The Model for Prediction Across Scales–Atmosphere (MPAS-A) solves the fully compressible, nonhydrostatic equations of atmospheric motion formulated in a height-based, hybrid terrain-following vertical coordinate (Skamarock et al., 2012, 2018). The horizontal discretization is implemented on an unstructured centroidal Voronoi mesh with C-grid staggering, in which horizontal velocity components are defined on cell edges, while other prognostic variables are located at cell centers. This unstructured mesh framework supports both global and regional simulations with quasi-uniform or variable-resolution meshes, allowing local refinement in targeted regions. In this study, forecasts are conducted with the MPAS-A Version 8.2.2 to evaluate its performance in simulating clouds over the Maritime Continent with two microphysics schemes: WSM6 and NSSL. Under a comparable configuration, the Thompson scheme has been shown to yield systematically lower precipitation forecast skill than WSM6 and NSSL (Chen et al., 2026) and is therefore excluded from the present evaluation.

WSM6 is widely used among microphysics schemes because of its high computational efficiency (Hong and Lim, 2006; Comin et al., 2018). Several studies have shown that WSM6 outperforms some other single-moment schemes in simulations of high-impact weather events, including tropical cyclones and organized convection (Kanase et al., 2015; Park et al., 2019; Huang et al., 2019a, b, 2020; Huo, 2024). Nevertheless, Sunny Lim et al. (2020) reported that WSM6 tends to overestimate precipitation in shallow cloud systems due to excessive cloud-ice production associated with deposition processes. Similar to WSM6, the NSSL scheme is a bulk microphysics parameterization that predicts the same five hydrometeor species—cloud water (Qc), rain (Qr), cloud ice (Qi), snow (Qs), and graupel (Qg). However, NSSL extends the single-moment framework to a double-moment formulation by additionally prognosing hydrometeor number concentrations, thereby enabling a more flexible representation of particle size distributions and associated microphysical processes (Mansell et al., 2010). Previous studies have demonstrated that the NSSL scheme exhibits superior performance in simulating cloud-base height, ice water content, and heavy-precipitation events compared with some single- and double-moment schemes (Gevorgyan, 2018; Wang, 2022; Nam, 2024). Although multi-moment microphysics schemes generally outperform single-moment schemes in representing size-sorting sedimentation and complex microphysical processes (Dawson et al., 2010; Milbrandt and McTaggart-Cowan, 2010; Wang et al., 2022), these advantages are not universally realized. Indeed, several studies have reported only limited improvements relative to single-moment schemes (Van Weverberg et al., 2013, 2014; Igel et al., 2015; Cho et al., 2020; Li et al., 2020; Luo et al., 2024).

In light of these differences, comparative forecast experiments are conducted to assess the performance of two representative bulk microphysics schemes, namely WSM6 and NSSL, in simulating tropical cloud systems within the MPAS framework. Although both schemes predict the same set of hydrometeor species, their underlying parameterizations differ substantially (Hong and Lim, 2006; Mansell et al., 2010). In the NSSL scheme, particle size distributions are formulated using gamma functions of particle diameter or volume, whereas WSM6 assumes exponential size distributions with prescribed intercept parameters. Heterogeneous ice nucleation in WSM6 is parameterized as a temperature-dependent process, with ice

https://doi.org/10.5194/egusphere-2026-1476
Preprint. Discussion started: 18 June 2026

crystal number concentration diagnosed as a function of the ice mass field (Hong et al., 2004). In contrast, the NSSL scheme adopts the parameterizations of Ferrier (1994) and Meyers et al. (1992) for the initiation of pristine ice crystals.

The configuration of other physical parameterization schemes is summarized in Table 1. Cloud fraction is diagnosed using the Xu–Randall scheme, in which subgrid-scale cloudiness is parameterized as a function of grid-mean cloud water mixing ratio and relative humidity (Xu and Randall, 1996). The model domain, centered over Singapore (1.21° N, 102.0° E), covers a radius of approximately 1,120 km with a quasi-uniform horizontal resolution of 3 km, comprising 522,172 grid cells (Figure 1). The vertical grid consists of 65 model levels extending from the surface to 40 km. Twelve 48-h cold-start forecasts, initialized at 00:00 and 12:00 UTC, are conducted during two convective episodes from 26 to 28 September and from 3 to 5 October 2024 (Chen et al., 2026). ECMWF HRES analyses and the corresponding forecasts are interpolated onto the MPAS mesh to generate the initial and lateral boundary conditions for each cold-start forecast.

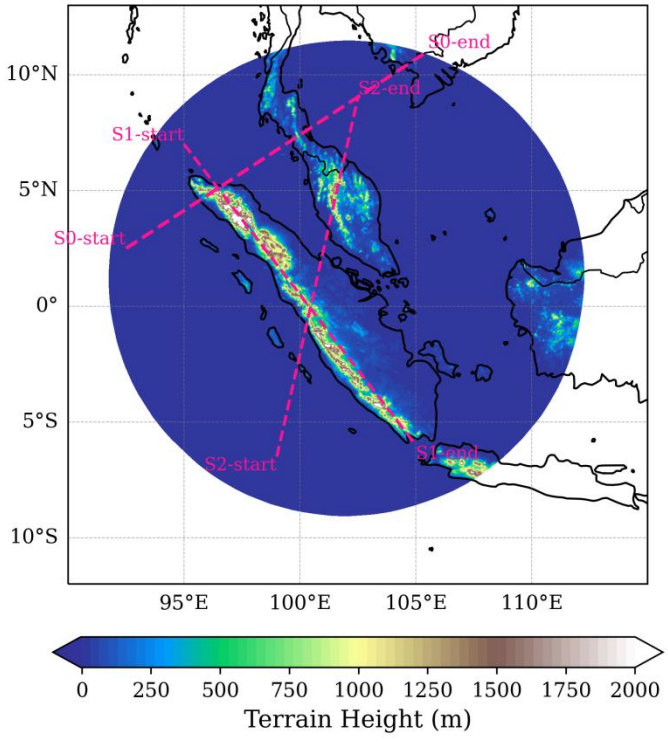

Figure 1. The terrain height (units: m) of MPAS simulation domain over the Maritime Continent, with three transects (S0–S2) used for subsequent cross-sectional analyses.

Table 1. MPAS Physics Configuration

Physics process	configuration
Boundary layer	MYNN

https://doi.org/10.5194/egusphere-2026-1476
Preprint. Discussion started: 18 June 2026

Surface layer	MYNN
Microphysics	WSM6 / NSSL
Convection	Grell-Freitas
Land surface	Noah
Shortwave/longwave Radiation	RRTMG
Cloud fraction for radiation	Xu-Randall
Gravity wave drag	YSU

2.2 Himawari-9 AHI Radiances and Retrieval Products

The Himawari-9 geostationary meteorological satellite, operated by the Japan Meteorological Agency (JMA), was launched on 2 November 2016 and became operational on 13 December 2022, when it succeeded Himawari-8. Its onboard Advanced Himawari Imager (AHI) provides full-disk observations every 10 min and regional imagery at temporal resolutions ranging from 2.5 min to 30 s, with spatial resolutions of 0.5 km in the visible bands and 2 km in the infrared bands. These high-frequency, high-resolution observations enable detailed analyses of cloud evolution and model performance.

Table 2 summarizes the key characteristics of AHI infrared channels 7–16, spanning wavelengths from 3.9 to 13.3 μm. AHI channel 7 (3.9 μm), located in the shortwave IR window, is sensitive to cloud phase and particle size variations and is widely used for nighttime cloud and fog detection, as well as low-level cloud identification. The water-vapor absorption bands (channels 8–10; 6.2, 6.9, and 7.3 μm) are primarily sensitive to mid- to upper-tropospheric humidity and cloud-top properties under cloudy conditions. The atmospheric-window bands 13–15 (10.4, 11.2, and 12.4 μm) are commonly applied in operational analyses for cloud-phase discrimination, low-level moisture monitoring, volcanic ash detection, and sea surface temperature retrieval, thereby supporting real-time NWP applications (Wang et al., 2018). In addition to channel 11 (8.6 μm), which is sensitive to cloud phase, the brightness temperature difference (BTD) between 8.6 μm and 11.2 μm (channel 14) serves as a key discriminator for cloud-type classification, with positive values typically associated with ice clouds and negative values indicating clear-sky or altocumulus conditions (Nasiri et al., 2008). Channel 16 (13.3 μm), located within the CO_2 absorption band, is used to infer cloud-top height and the optical thickness of thin cirrus clouds (Bessho et al., 2016). In this study, cloud microphysical properties are evaluated through simulations of AHI infrared radiances from channels 7–16, excluding the ozone-sensitive channel 12 (9.6 μm), which lies beyond the scope of this analysis.

https://doi.org/10.5194/egusphere-2026-1476
Preprint. Discussion started: 18 June 2026

In addition to Level-1 radiance data, fundamental cloud products from Himawari-9, comprising cloud mask, cloud type, and cloud-top information, are also used for evaluation at the same high resolution. These products are generated using retrieval algorithms originally developed under the National Oceanic and Atmospheric Administration (NOAA) / National Environmental Satellite, Data, and Information Service (NESDIS) Enterprise project for the Geostationary Operational Environmental Satellite–R (GOES-R) Advanced Baseline Imager (ABI) (Imai et al., 2016). The binary cloud mask product is derived using the NOAA/NESDIS Enterprise Cloud Mask (ECM) methodology (Heidinger et al., 2018). Cloud-top-height is retrieved using the 13.3-μm CO_2 absorption band in combination with several longwave infrared window channels (10.4, 11.2, and 12.4 μm) (Heidinger et al., 2011, 2020). The cloud-type product is derived from four AHI infrared channels (7.3, 8.6, 11.2, and 12.4 μm) and classifies clouds into nine categories: fog, warm liquid water (WL), supercooled liquid water (SLW), mixed phase (MIXED), opaque ice (ICE), cirrus (semithin ice), overlap (with a semi-transparent upper layer), overshooting, and uncertain (UN) (Pavolonis et al., 2010; Pavolonis and Corey, 2020).

Table 2. Characteristics of Himawari-9 AHI infrared channels

Channel	Central wavelength (μm)	Spatial resolution (km)	Physical Properties
7	3.9	2	Low Cloud, Fog, Forest Fire
8	6.2	2	Mid- and Upper- Level Moisture
9	6.9	2	Mid-Level Moisture
10	7.3	2	Mid- and Lower- Level Moisture
11	8.6	2	Cloud Phase, Volcanic SO_2
12	9.6	2	Ozone and potential vorticity
13	10.4	2	Clouds, Cloud Top Information
14	11.2	2	Clouds, Sea Surface Temperature
15	12.4	2	Clouds, Sea Surface Temperature
16	13.3	2	Cloud top height, CO2

https://doi.org/10.5194/egusphere-2026-1476
Preprint. Discussion started: 18 June 2026

206

2.3 Radiance Simulation with MPAS-JEDI and CRTM

This study uses the MPAS-JEDI system to perform all-sky radiance simulations over the model domain (Figure 1) and to compare the simulations with Himawari-9 AHI radiance observations. MPAS-JEDI (Liu et al., 2022; Guerrette et al., 2023; Jung et al., 2024; Sun et al., 2025) is a new-generation data assimilation system for MPAS-A, developed within the Joint Effort for Data assimilation Integration (JEDI) framework (Trémolet and Auligné, 2020). While MPAS-JEDI supports the assimilation of microwave and infrared radiance observations through the Community Radiative Transfer Model (CRTM) as the radiance observation operator (Liu and Weng, 2006; Chen et al., 2008; Johnson et al., 2023), this study applies the so-called *HofX* capability to forward-simulate AHI BTs from MPAS forecast outputs and to directly compare them with observations. To facilitate model–observation comparisons, hourly full-disk AHI radiance data and cloud products are remapped onto the regional MPAS unstructured mesh and converted into the Interface for Observation Data Access (IODA) format, which can be directly ingested by the MPAS-JEDI *HofX* application. In this study, CRTM version 2.4.1 is employed to simulate AHI radiances under all-weather situations using geophysical inputs from MPAS forecasts, including profiles of pressure, temperature, water vapor, the mixing ratios and effective radii of five hydrometeor species: cloud liquid water, cloud ice, rain, snow, and graupel. Surface emissivity is handled by the CRTM surface module, which accounts for four major surface types, including water, land, ice, and snow (Johnson et al., 2023).

3 Evaluation of Cloud Forecast

Based on AHI radiances and retrieval products, cloud representations in the WSM6 and NSSL microphysics schemes are examined from multiple perspectives, including cloudy-sky radiance simulations, cloud properties, and their diurnal evolution. A two-dimensional horizontal comparison is conducted between model-simulated and observed cloud states for each mesh cell. Model grid cells are classified as cloudy following the ECMWF diagnostic criterion, whereby the cloud fraction exceeds 1% and the total condensate of cloud liquid and ice is greater than 1×10^{-6} kg kg^{-1} (Serra et al., 2023). The observed cloudiness is determined using the AHI cloud mask, in which a value of 1 denotes cloudy conditions and 0 represents clear sky. The comparison results are presented in the following subsections.

3.1 Cloudy-Sky Radiance Simulation

Figure 2 presents the BT probability distributions of nine AHI infrared channels for the observations and for simulations using the two microphysics schemes. The statistics are derived from cloud-matched samples jointly identified by the observations and each microphysics scheme. Given the comparable numbers of matched cloudy samples, with 17,184,742 matched samples for OBS-WSM6 and 17,238,036 for OBS-NSSL, the observational distributions show negligible differences between the two matching procedures, as shown in Figures 2a and 2c shown. For brevity, the observational results presented in the following sections are shown only for samples matched with the WSM6 simulations.

https://doi.org/10.5194/egusphere-2026-1476
Preprint. Discussion started: 18 June 2026

The observed AHI BTs exhibit pronounced inter-channel variability (Figures 2a and 2c), consistent with their spectral sensitivities summarized in Table 1. The water-vapor bands 8–10 show relatively narrow BT ranges with broad, high-frequency peaks between ~210–260 K, reflecting the prevalence of moisture in the middle to upper troposphere. Besides, the IR window channels 11 and 14–16 display a substantially broader BT range (~210–290 K) with similar frequency structures. The warm-side distribution of channel 13 (10.4 μm), a relatively "cleaner" IR window band, is shifted toward cooler BTs (~220–270 K) owing to reduced water-vapor attenuation and increased sensitivity to high cloud-top emission (Lindsey et al., 2012). Meanwhile, channel 7 (3.9 μm), which is strongly sensitive to low-level clouds, fog, and surface emission, yields the warmest and most right-skewed BT distribution among the AHI infrared channels.

Relative to the observations, both WSM6 and NSSL simulations reproduce the overall inter-channel hierarchy, yet exhibit notable differences in distribution width, frequency structure, and cold-tail characteristics. For the water-vapor channels (8–10), WSM6 more closely matches the observed BT distributions, whereas NSSL exhibits larger departures, characterized by an expanded distribution toward colder BTs and a weakened warm-side peak. For the window channels (11 and 14–16), the observed BT span of 210–290 K is more realistically captured by NSSL, although it features an extended cold tail around 200–210 K. This pronounced cold tail in the NSSL simulations indicates an overabundance of high-level clouds. Comparatively, WSM6 better reproduces the overall frequency structure, but its underestimation of cold BTs suggests insufficient high or optically thick cloud representation. Unlike the observed channel 13, which exhibits a distinctly narrower BT range and higher-frequency distribution, the simulated BTs from both WSM6 and NSSL fail to reproduce this feature, implying limited skill in representing cloud-top radiative signatures. Moreover, both microphysics schemes exhibit a larger frequency of warm BTs around 280–295 K relative to the observations. This bias may be associated with insufficiently opaque low-level clouds in the simulations (Wang et al., 2013), whereby clouds exist in terms of condensate mass and cloud fraction but are radiatively too thin to effectively block surface thermal emission in the window channels (Wang et al., 2013). Lastly, verification against nighttime channel 7 (3.9 μm) observations indicates that NSSL aligns more closely with the observed BT distribution, implying a more realistic simulation of low-level clouds or fog compared with WSM6.

https://doi.org/10.5194/egusphere-2026-1476
Preprint. Discussion started: 18 June 2026

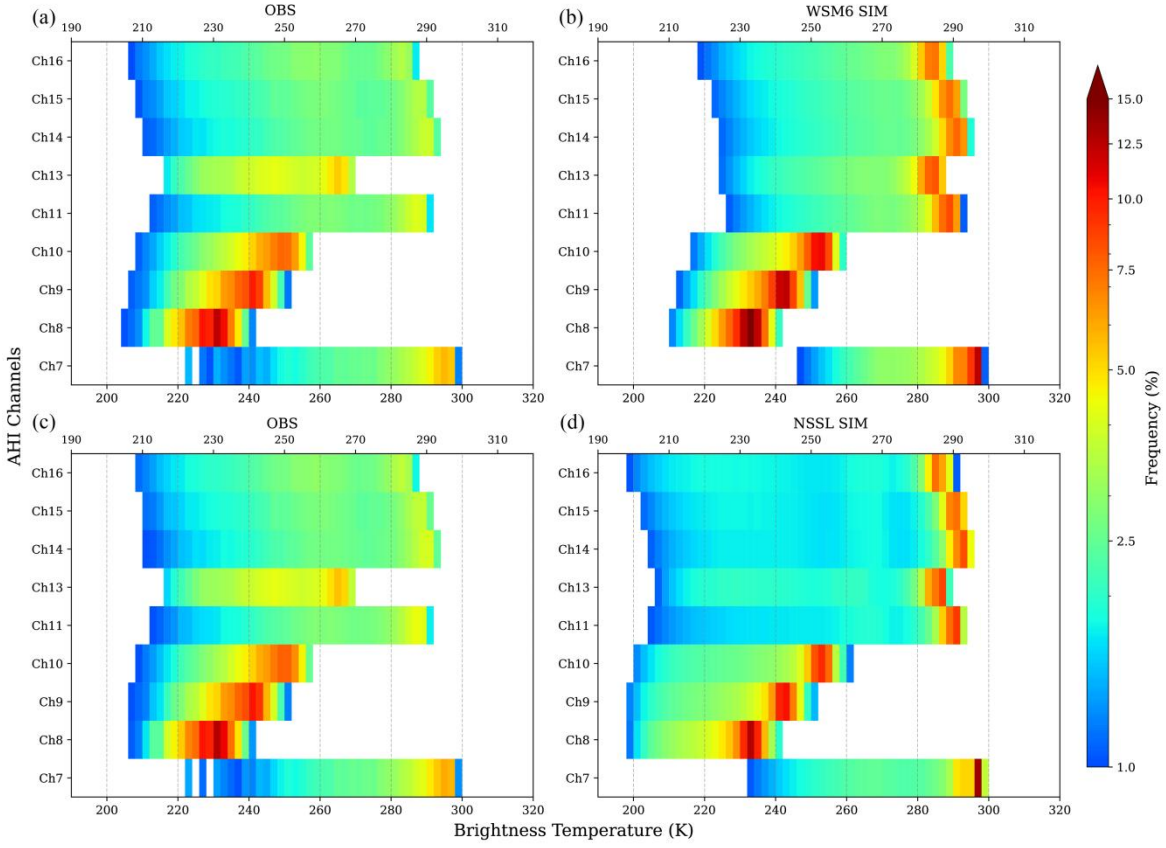

Figure 2. Frequency distributions (>1.0%) of AHI brightness temperatures (BTs; K) for channels 7–11 and 13–16 from (a, c) observations cloud-matched with WSM6 and NSSL, respectively, and the corresponding (b) WSM6 and (d) NSSL simulations. Statistics are computed from 24-48 h forecasts at 6 h intervals, except for channel 7 using only nighttime samples (12-18 h and 36-42h; 20:00-02:00 SGT).

As a representative convective-cloud case at 12:00 UTC on 5 October 2024, Figure 3 illustrates the differences between WSM6 and NSSL through a comparison of observed and model-simulated AHI channel 13 BTs, together with the corresponding vertical distributions of cloud fraction, hydrometeors, relative humidity, and vertical velocity along the S0 transect shown in Figure 1. The AHI channel 13 observations exhibit pronounced spatial variability, with several cold minima below 230 K and corresponding cloud-top pressures lower than ~150 hPa (Figures 3a-b), characteristic of deep convective clouds (Wall et al., 2018). Overall, WSM6 simulates warmer BTs, whereas NSSL produces colder values that are closer to the observations, particularly over convective regions (Figures 3a-b). Over the eastern portion of the transect (~103°–106° E), however, WSM6 shows better agreement with the observations than NSSL, suggesting a more realistic representation of hydrometeors (Figures 3a-b).

Further diagnosis of hydrometeors and cloud fraction helps elucidate the sources of the BT differences between the two schemes (Figures 3c-d). In WSM6, upper-tropospheric Qi and Qs are scarce above ~400 hPa, indicating limited ice growth aloft, whereas larger amounts of Qc and Qr are concentrated near the melting layer, implying more efficient warm cloud

https://doi.org/10.5194/egusphere-2026-1476
Preprint. Discussion started: 18 June 2026

processes. Consistently, cloud fraction remains sparse above 250 hPa and increases primarily within the 300–500 hPa layer. Hence, the larger positive forecast-minus-observation (F–O) BT biases in WSM6 are associated with those optically thinner upper-level anvils and enhanced infrared emission from lower-level clouds. In contrast, abundant cloud amounts and ice-phase hydrometeors (Qi and Qs) are evident in NSSL from ~500 hPa to the upper troposphere, implying thicker high-level clouds and leading to colder simulated BTs that are closer to the observations. It is also noteworthy that the observed cloud-top heights are lower than those simulated by both schemes. Such discrepancies likely stem from excessive condensate lofting through enhanced updrafts (Pandey et al., 2023). Besides, thermodynamic differences between the two schemes are reflected in the vertical distributions of vertical velocity and relative humidity, rather than in their magnitudes (Figures 3e-f). In WSM6, the core of upward motion is generally confined to lower altitudes near the melting layer (Figure 3e), favoring warm-phase processes and the development of lower-level clouds. By contrast, NSSL exhibits a deeper and higher ascent core, accompanied by a near-saturated moisture environment (Figure 3f), which probably facilitates the ice growth and anvil development.

https://doi.org/10.5194/egusphere-2026-1476
Preprint. Discussion started: 18 June 2026

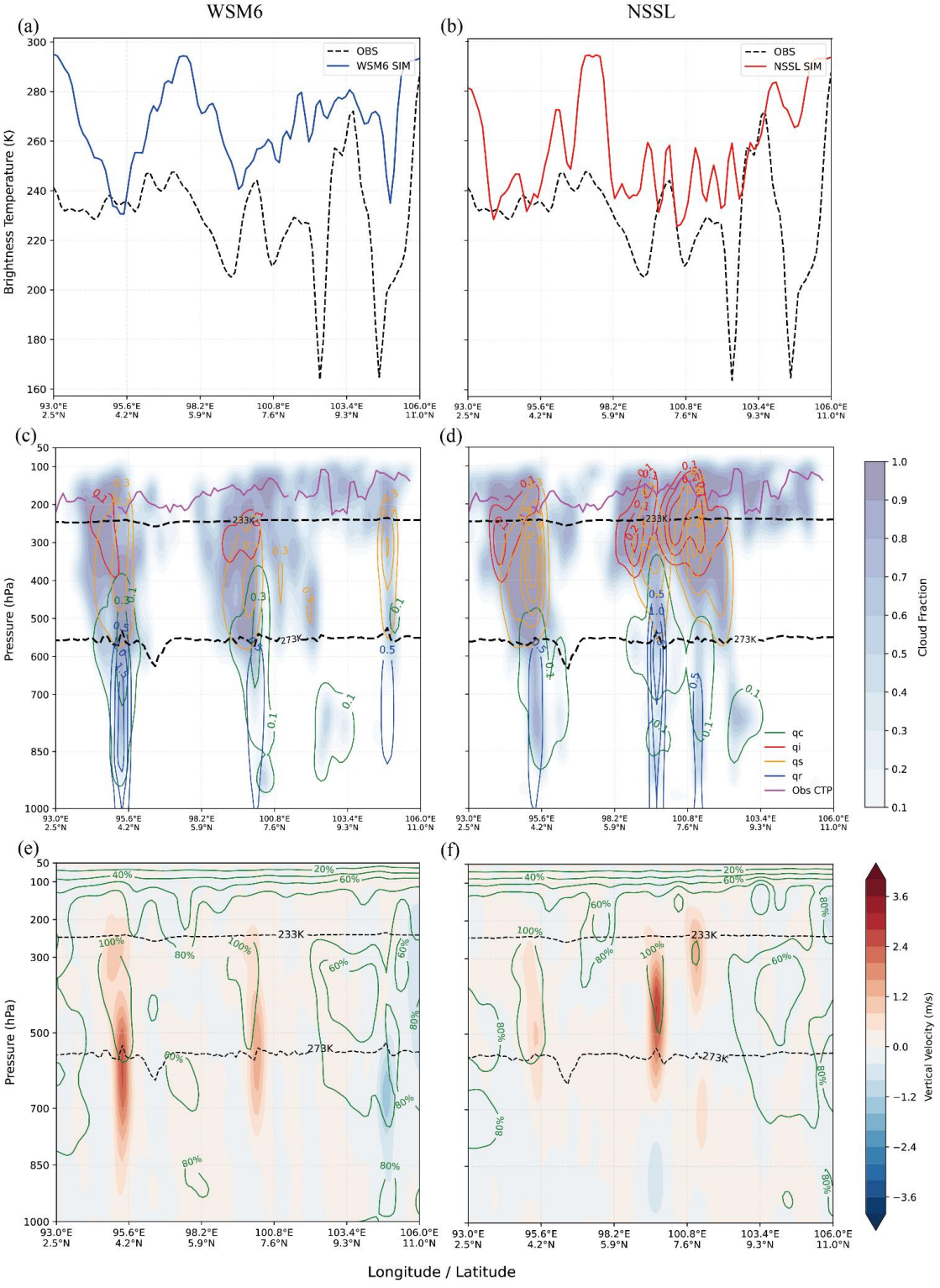

https://doi.org/10.5194/egusphere-2026-1476
Preprint. Discussion started: 18 June 2026

Figure 3. (a, b) AHI channel 13 brightness temperatures (BTs; units: K) along the S0 transect shown in Figure 1 from observations (black dashed), simulations of WSM6 (blue) and NSSL (red) for a representative convective case, and the corresponding vertical cross sections of (c, d) cloud fraction (shading), and mixing ratios exceeding 0.1 g/kg for cloud liquid water (qc), cloud ice (qi), snow (qs), and rain (qr) (contours, units: g/kg), and (e, f) vertical velocity (shading, units: m s^{-1}) and relative humidity (green contours, units: %) for WSM6 (left panels) and NSSL (right panels) for a 12 h forecast valid at 12:00 UTC on 5 October 2024. Purple solid lines in (c–d) denote observed cloud-top pressure, and black dashed lines in (c–f) mark the 273 and 233 K isotherms.

3.2 Cloud Amount, Cloud Type and Cloud-Top-Height

To evaluate the model performance in representing cloudiness, two metrics are used to quantify cloud-amount forecast skills: the Critical Success Index (CSI) and Negative Probability of Detection (PODN), which are formulated as follows (Grecu and Krajewski, 2000),

$$\mathrm{CSI} = \frac{\mathrm{Na}}{\mathrm{Na} + \mathrm{Nb} + \mathrm{Nc}}, \tag{1}$$

$$\mathrm{PODN} = \frac{\mathrm{Nd}}{\mathrm{Nb} + \mathrm{Nd}}. \tag{2}$$

Here, Na denotes the number of grid cells identified as cloudy by both MODEL and OBS (hits), Nb represents the number of grid cells classified as cloudy by MODEL but clear by OBS (false alarms), Nc refers to the number of grids identified as clear by MODEL but cloudy by OBS (misses), and Nd indicates the number of grids recognized as clear by both OBS and MODEL (correct negatives). These contingency relationships between observed and model cloudiness states are summarized in Table 3. For each metric, values approaching 1.0 indicate higher cloud forecast skill and closer agreement between the model and observations.

Figures 4c-d present CSI and PODN for the cloudiness forecast as a function of forecast lead time (Singapore local time) for WSM6 and NSSL. Besides, Figures 4a-b present the numbers of cloudy and clear-sky pixels identified separately by the observations and by the model with each microphysics scheme. It is noted that both schemes tend to overpredict cloudy pixels and underpredict clear-sky pixels relative to the observations. These mismatched samples primarily correspond to "Oclear-Mcloud" situations, indicating inconsistencies between the model-simulated and observed cloudiness states.

As shown in Figures 4a-b, the observations indicate that cloud amount reaches its maxima during forecast hours 9–18 and 33–42 (17:00–02:00 SGT) and decreases to minima during forecast hours 21–27 and 45–48 (05:00–11:00 SGT). Both WSM6 and NSSL reproduce the overall temporal evolution, although the model simulated cloud maxima occurs relatively later than observed when the observed cloud amount peaks around 9 h and 33 h (Figure 4a). Consistently, the CSI for both schemes increases markedly during 9–21 h and 30–45 h (17:00–05:00 SGT), with pronounced declines around 21–27 h and 45–48 h (05:00–11:00 SGT; Figure 4c). These fluctuations closely coincide with the diurnal variation in cloudy-pixel counts shown in Figure 4a. In other words, cloud representation skill is higher during periods of cloud development and lower during cloud dissipation. Moreover, during the first 9 h, NSSL produces fewer cloudy pixels and more clear-sky pixels, in closer agreement with the observations, suggesting a more realistic spin-up of initial cloud development (Figure 4a). In contrast, WSM6 tends to overpredict cloud occurrence, with a subset of observed clear-sky pixels being erroneously classified as cloudy.

https://doi.org/10.5194/egusphere-2026-1476
Preprint. Discussion started: 18 June 2026

Correspondingly, higher CSI and PODN scores are achieved by NSSL within the first 9 h (Figures 4c-d). At later forecast times beyond 24 h, although the total counts of cloudy and clear-sky pixels simulated by WSM6 become closer to the observations, its CSI score remains lower than that of NSSL. This likely reflects the persistence of larger spatial displacement errors in the WSM6 cloud forecasts, despite improved agreement in the overall cloud counts. NSSL maintains higher CSI values, reaching approximately 0.86 near 45 h (Figure 4c), suggesting an improved hit rate and fewer false alarms under cloudy conditions.

In terms of the PODN metric, both schemes exhibit consistently low values below 0.5 (Figure 4d), indicating that clear-sky scenes are frequently misclassified as cloudy. Nevertheless, the higher PODN values obtained with NSSL, especially for the first 24 h, indicate a better representation of clear-sky scenes compared with WSM6. The gradual decrease in PODN after 12 h is consistent with the growing discrepancy between simulated and observed clear-sky sample counts (Figures 4b and 4d). Overall, NSSL demonstrates superior skill in representing cloud occurrence, particularly in terms of spatial consistency with the observed cloud fields, whereas the WSM6 shows larger spatial displacement errors of clouds and reduced skill in discriminating between cloudy and clear-sky conditions during the spin-up period.

Table 3. Contingency table for binary cloud-amount forecast accuracy metrics

	Model Cloud (Mcloud)	Model Clear (Mclear)
Obs Cloud (Ocloud)	Na (Hits)	Nc (Misses)
Obs Clear (Oclear)	Nb (False Alarms)	Nd (Correct Negatives)

https://doi.org/10.5194/egusphere-2026-1476
Preprint. Discussion started: 18 June 2026

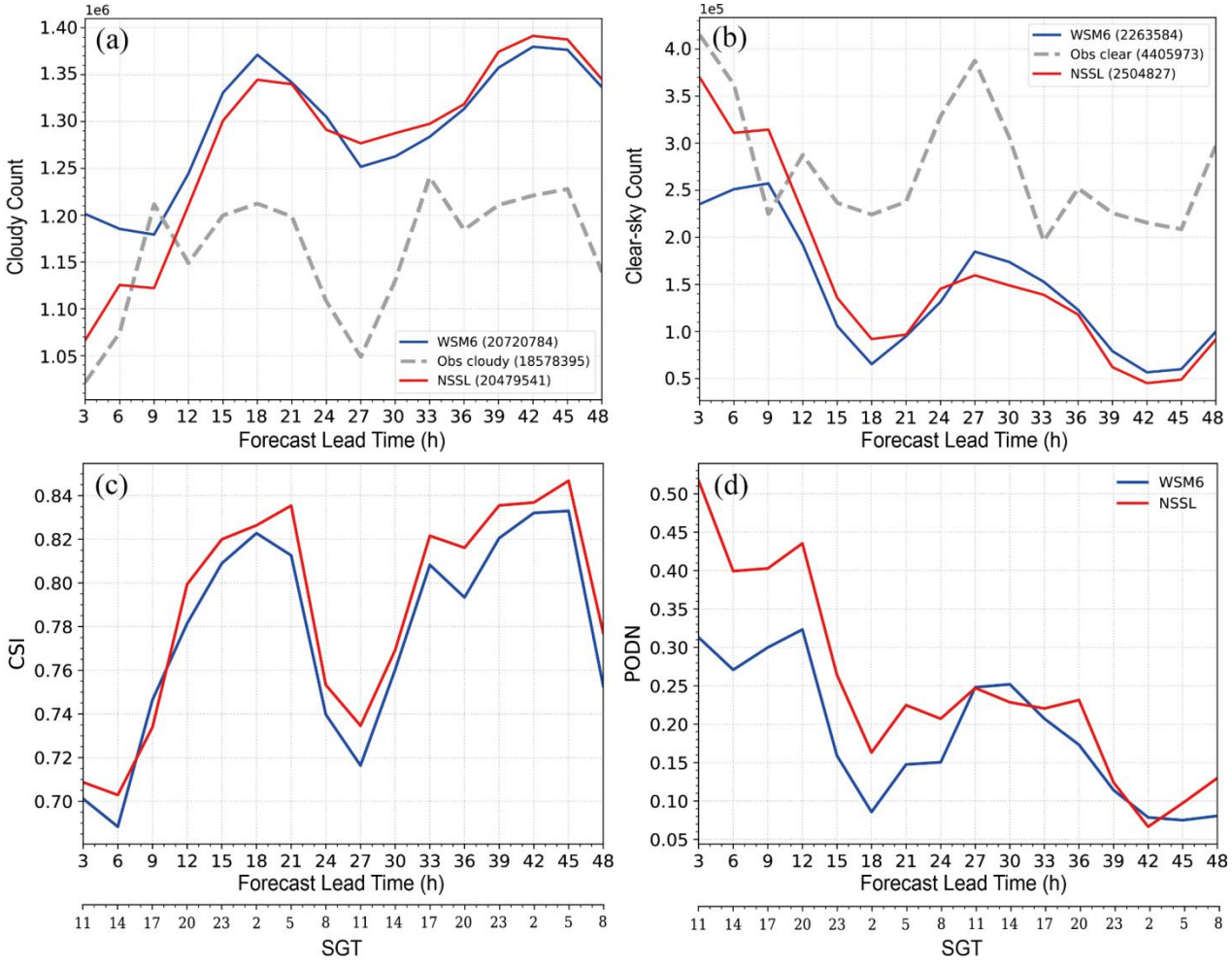

Figure 4. Observed and model-simulated (a) cloudy and (b) clear-sky pixels counts, along with (c) Critical Success Index (CSI) for cloud-amount forecast and (d) Probability of Detection for Non-cloud (PODN) as a function of forecast lead time. The forecasts are initialized at 00:00 UTC and the corresponding Singapore local times are also marked in the x-axis

The brightness temperature difference (BTD) of the ~8.5–8.7 μm minus the ~11 μm window channels can be used to effectively discriminate liquid and ice clouds because of differences in their radiative properties (Otkin et al., 2009; Menzel et al., 2015). Figure 5 illustrates the joint frequency distributions of the BTD of 8.6–11.2 μm ($BTD_{8.6\text{-}11.2}$) versus the 11.2 μm BT in the observations and model simulations for several distinct liquid- and ice-cloud types. During the study period, liquid-water clouds identified by AHI retrievals are relatively rare, accounting for ~5–6% of all cloudy samples, whereas ice clouds dominate, with optically thin and optically thick ice clouds comprising 45.9% and 21.2%, respectively. Supercooled liquid-water and mixed-phase clouds together account for only ~1–2% and are therefore excluded from the analysis. The scarcity of liquid-phase cloud samples likely reflects an inherent limitation of passive infrared sensors, which are primarily sensitive to the uppermost cloud layer, such that liquid clouds may be obscured by overlying ice clouds and are therefore underrepresented in IR-based cloud-type retrievals (Haynes et al., 2022).

https://doi.org/10.5194/egusphere-2026-1476
Preprint. Discussion started: 18 June 2026

The observed frequency distribution exhibits a high-frequency core (> 1.0%) spanning BTs of 200-290 K and $BTD_{8.6\text{-}11.2}$ from −4 K to 5 K (Figures 5a-c). The positive $BTD_{8.6\text{-}11.2}$ value corresponds to ice-phase clouds, resulting from the reduced emissivity of ice particles at 11.2 μm relative to 8.6 μm (Figures 5b-c). In contrast, liquid water clouds generally yield $BTD_{8.6\text{-}11.2} < 0$ with 11.2 μm BTs in the range of 240-290 K, reflecting their higher emissivity at 11.2 μm compared with 8.6 μm (Figure 5a). Moreover, under cloudy conditions, lower 11.2 μm BTs (< 240 K) indicate optically thicker clouds or higher altitude clouds, often associated with deep convection, whereas higher BTs (> 260 K) generally correspond to optically thinner or lower altitude clouds.

Relative to the observations, the overall BTD–BT pattern in the low-frequency regime (< 1.0%) is noticeably broadened in both schemes (Figures 5d-i), indicating increased uncertainty in the prediction of low-frequent cloud states. The extended $BTD_{8.6\text{-}11.2}$ tails exceeding 15 K in both simulations are likely associated with the presence of semi-transparent ice clouds, which amplify extinction differences between 8.6 and 11.2 μm (Mayer et al., 2024). Besides, the ice cloud distribution produced by WSM6 is systematically shifted toward larger positive BTDs when the observed peak occurrence falls within ~200–260 K of 11.2 μm BTs and -5–0 K of BTDs (Figures 5b-c and 5e-f), suggesting biases in the simulated optical and microphysical properties of those ice clouds.

In the high-frequency core (frequency > 1.0%), the observed BTD distribution for liquid-water clouds is well captured by both experiments, although the occurrence of colder liquid-water cases (BT < 280 K) is underpredicated (Figures 5a, 5d and 5g). It is also noted that WSM6 overpredicts the frequency within the 0–5 K BTD range (Figure 5d), which may be attributable to misclassification between liquid- and ice-phase cloud categories. For optically thin ice clouds, WSM6 more accurately predicts the observed frequency structure within the BT range of 220–290 K and BTDs of −2 to 5 K (Figures 5b and 5e). In contrast, NSSL underpredicts the frequency within the BT range of 260–280 K and $BTD_{8.6\text{-}11.2}$ of 0–5 K in this thin ice regime (Figures 5b and 5h). Despite these differences, both schemes show improved performance for optically thin ice clouds relative to other ice-cloud regimes. Under thick ice conditions, frequencies within the 200–240 K BT range are substantially underpredicted in the WSM6 simulations (Figures 5c and 5f). Although NSSL shows better agreement with observations along the BT axis within 200–240 K, its frequency distribution exhibits excessive extension toward both large negative and positive BTD values (Figures 5c and 5i). Overall, the phase-dependent structure in BTD space is generally in good agreement between the observations and both schemes, whereas larger discrepancies are evident along the BT axis, implying greater uncertainties in the prediction of cloud-top characteristics than in the split-window radiative response.

https://doi.org/10.5194/egusphere-2026-1476
Preprint. Discussion started: 18 June 2026

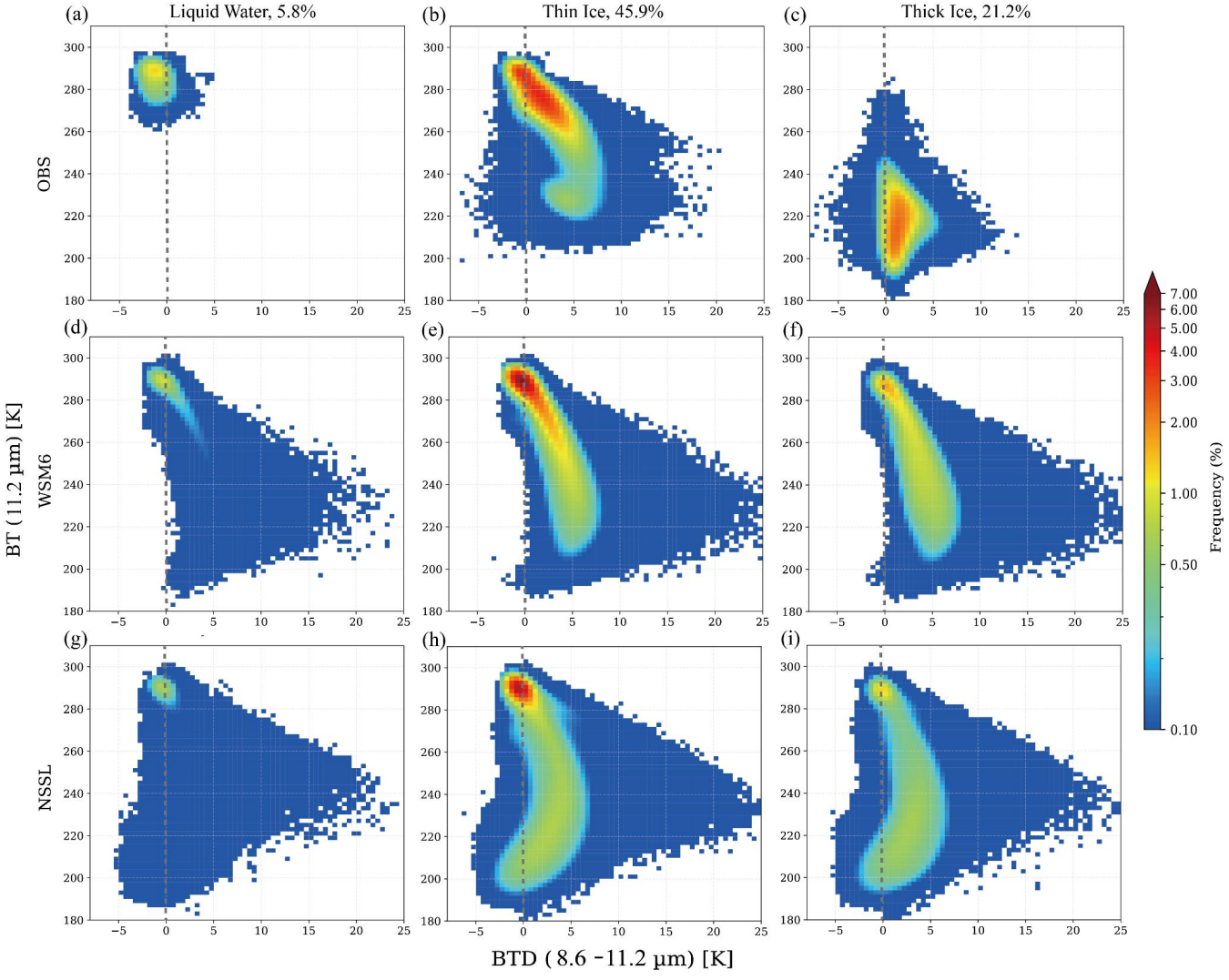

Figure 5. Frequency distributions (> 0.1%) of 8.6–11.2 µm (channel 11–14) brightness temperature differences (BTDs, units: K) versus 11.2 µm (channel 14) brightness temperatures (BTs, units: K) under different AHI L2 cloud-type conditions, including liquid water clouds (first column), thin ice clouds (second column), and thick ice clouds (third column), shown for (a-c) observations, (d-f) WSM6 simulations, and (g-i) NSSL simulations. Statistics are calculated using cloud-matched samples and binned at 0.5 K intervals for BTD and 2 K intervals for BT, based on 24-48 h forecasts with a 6 h interval.

Figure 6 presents the joint frequency distributions of cloud-top pressure (CTP) versus the cloud-top sensitive AHI channel 16 BTs for the observations and for the WSM6 and NSSL simulations. In the model, cloud top is diagnosed following the methodology of the ECMWF Integrated Forecasting System (ECMWF, 2024) and is defined as the uppermost level of consecutive cloudy layers within each column. As shown in Figure 6a, the observed distribution exhibits a clear inverse relationship between CTP and BT, with higher BTs corresponding to lower cloud-top pressures. The highest observed CTP frequencies are concentrated between 150 and 350 hPa for BTs ranging from 200 to 260 K, indicative of abundant deep convective anvils. In addition, a weaker but distinct branch extends downward to layers near 900 hPa with BTs of

https://doi.org/10.5194/egusphere-2026-1476
Preprint. Discussion started: 18 June 2026

approximately 260–270 K, representing the presence of lower-level clouds. Both WSM6 and NSSL reproduce the overall inverse CTP-BT relationship, yet exhibit systematic biases in high-cloud representation (Figures 6b-c). In both schemes, simulated CTP frequencies are concentrated primarily between 100 and 200 hPa, with much lower occurrences between 250 and 600 hPa, indicating that cloud tops are generally simulated at higher altitudes than observed. For upper-level clouds at 150–200 hPa, the NSSL scheme more accurately reproduces the observed BT distribution. However, it also exhibits an expanded high-frequency occurrence of BTs near 220 K above 150 hPa (Figure 6c), suggesting an overprediction of optically thick high-level ice clouds. This feature is consistent with the broader high-frequency distributions simulated by NSSL (Figure 5i) relative to the observations (Figure 5c). Additionally, the WSM6 scheme shows more pronounced BT biases for high clouds, characterized by an underprediction of colder BTs and an overprediction of warmer BTs above 200 hPa (Figure 6b), implying a less realistic representation of high-cloud optical thickness. Furthermore, both schemes underpredict the frequency of clouds below approximately 600 hPa at BTs of 260–270 K, characteristics of mid- to low- levels clouds.

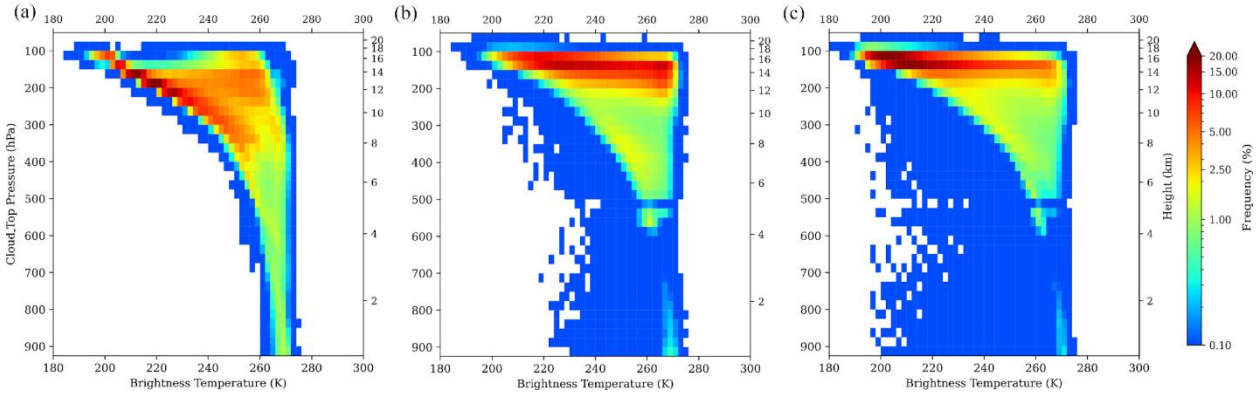

Figure 6. Frequency distributions (> 0.1%) of cloud top pressure (CTP, units: hPa) versus Channel 16 (13.3 μm) brightness temperature (BT, units: K) for (a) observations, (b) WSM6 and (c) NSSL simulations. Statistics are computed within binned intervals of 25 hPa in CTP and 2 K in BT. Model data are from 24-48 h forecasts with a 6 h interval.

3.3 Diurnal Variation of Cloud Forecast

Figure 7 displays the probability distributions of channel 13 F–O BTs as a function of forecast lead time for the WSM6 and NSSL schemes under different cloud-type conditions. With asymmetric F–O distributions, we use median instead of mean to better characterize the primary bias tendency. For liquid-water clouds (5–6 % of total cloud samples), both schemes show relatively good consistency between simulated and observed BTs. The corresponding F–O distributions are tightly centered around zero and exhibit minimal temporal variability (Figures 7a-b). For optically thin ice clouds, representing about 45% of the total samples, this category is predicted most accurately by both schemes among all ice-cloud types. This behavior is characterized by smaller F–O biases and lower standard deviations (STDs), particularly in WSM6 (Figures 7c-d). The comparatively larger F–O medians and STDs in NSSL are likely attributable to an underprediction of thin ice clouds, as illustrated by the cloud-type frequency distributions in Figures 5b and 5g. Under optically thick ice cloud conditions (Figures 7e-f), the contrast between the two schemes becomes more pronounced. NSSL exhibits clear superior performance, with a

https://doi.org/10.5194/egusphere-2026-1476
Preprint. Discussion started: 18 June 2026

substantially smaller warm bias (3.69 K) when compared to WSM6, which has an average warm bias of 25.01 K. The warm bias of WSM6 increases with forecast lead time (Figure 7e), consistent with its pronounced underprediction of thick ice cloud frequency shown in Figures 5c and 5f. Multilayered ice clouds (25.7% of total cloud samples) are simulated with the lowest skill in both schemes, as evidenced by broad probability plumes displaced from 0 K and the largest STDs among all cloud categories (Figures 7g-h). This discrepancy is further amplified in NSSL, which exhibits a wider bias range extending from −30 K to 30 K.

Overall, a diurnal variation of F–O is evident for both schemes, with particularly pronounced signals in NSSL under thick and multilayer ice cloud conditions. These signals are characterized by a tendency toward negative F–Os during the daytime periods of 6–9 h and 30–33 h (14:00–17:00 SGT), followed by a marked shift toward positive F–Os during the 12–21 h and 36–45 h nighttime hours (20:00–5:00 SGT, Figures 7f and 7h). Meanwhile, for both schemes, the STDs across different cloud types generally decrease during the daytime period (14:00–17:00 SGT), accompanied by a more concentrated distribution of F–O samples. In contrast, larger STDs and more dispersed F–O distributions are observed during the nighttime period (20:00–05:00 SGT). The underlying mechanisms responsible for these diurnal characteristics are further examined in following sections.

https://doi.org/10.5194/egusphere-2026-1476
Preprint. Discussion started: 18 June 2026

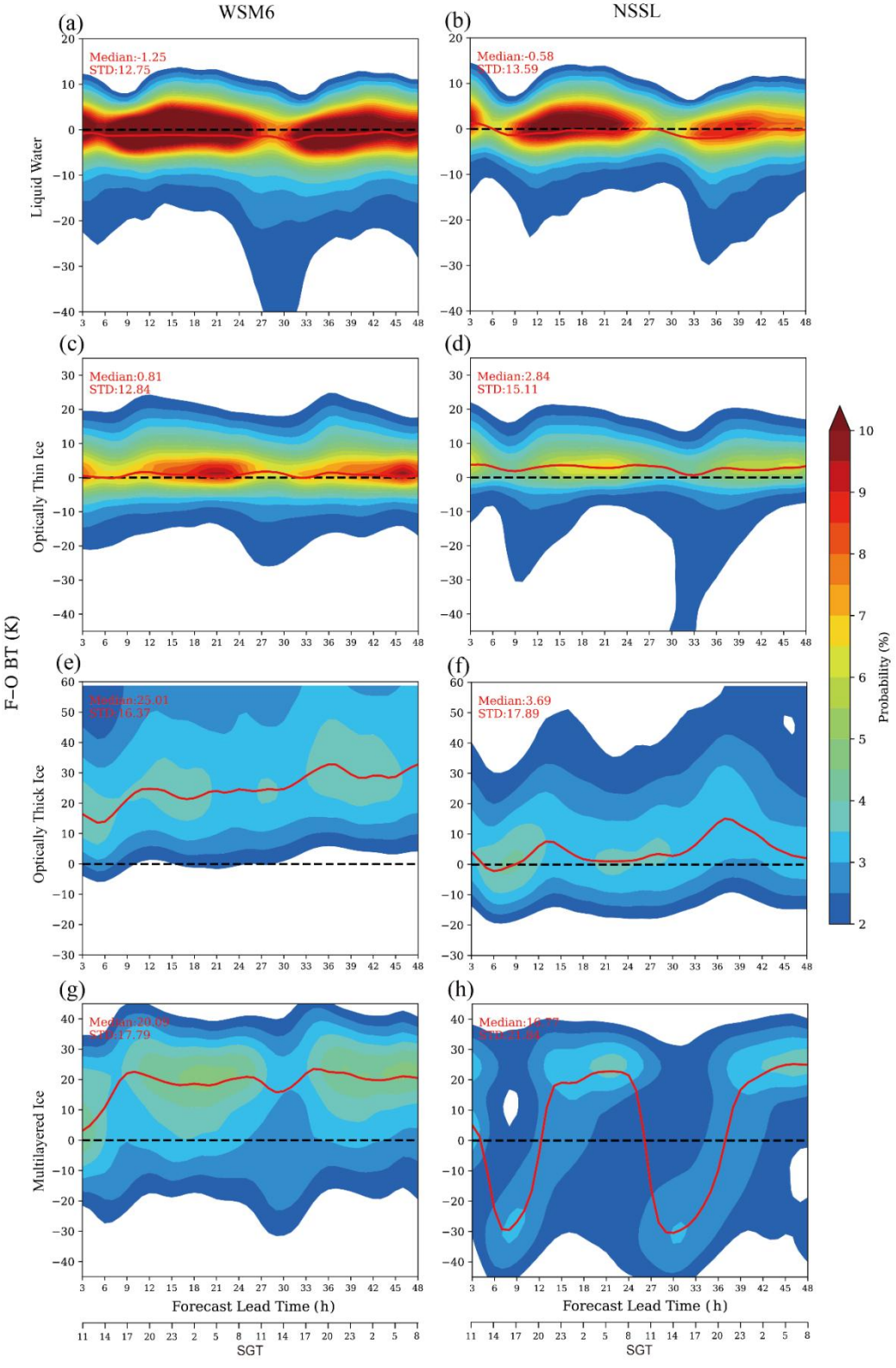

https://doi.org/10.5194/egusphere-2026-1476
Preprint. Discussion started: 18 June 2026

Figure 7. Probability distributions of channel 13 Forecast-Minus-Observation brightness temperature (F–O BT; units: K) as a function of forecast lead time (from 00:00 UTC) for WSM6 (first column) and NSSL (second column) under four cloud-type conditions. Lead time-averaged median and standard deviation values of F–O are shown in each legend. The red line denotes the median values at different forecast ranges.

To further elucidate the diurnal mechanisms from a microphysical perspective, Figure 8 presents the domain-averaged cloud fractions and hydrometeor mixing ratios as functions of forecast lead time and pressure level for the WSM6 and NSSL schemes. Compared with NSSL, WSM6 exhibits smaller cloud fractions (< 0.4) and thinner anvil layers between 250 and 100 hPa, whereas NSSL produces deeper anvils with larger cloud fractions (> 0.6) extending from 100 to 350 hPa (Figure 8a). Besides, a large amount of Qc in WSM6 is concentrated within the mixed-phase layer near the 273 K isotherm, exhibiting two distinct peaks during the nocturnal periods of 15–24 h and 39–48 h. Subsequently, Qc near 273 K appears to be preferentially depleted through riming and accretion processes, whereby supercooled Qc is likely collected and frozen by ice particles to enhance Qg, while Qc is possibly accreted by raindrops, leading to increased Qr. This conversion is evidenced by notable increases in Qg (up to ~0.035 g kg^{-1} between 400 and 600 hPa) and Qr (up to ~0.030 g kg^{-1} below 600 hPa). The enhanced efficiency of riming and accretion in WSM6 is likely associated with the lower altitude of the saturation-layer top (RH = 100%) near 400 hPa, which facilitates supersaturation and intensified liquid–ice interactions. Under these conditions, enhanced mid-level Qc and Qg near the melting layer (~273 K) may contribute to the reduced F–O biases and smaller STDs for liquid-water clouds in WSM6 (Figures 7a, 8a, and 8c). In contrast, upper-tropospheric Qi and Qs in WSM6 remain nearly steady, with Qi ranging from 0.005 to 0.019 g kg^{-1} and Qs generally below ~0.035 g kg^{-1} above 500 hPa (Figures 8a and 8c), values that are clearly lower than those simulated by NSSL (Figures 8b and 8d). The lower saturation height in WSM6 likely suppresses depositional ice growth, resulting in thinner ice layers in the upper troposphere. This pattern is consistent with the reduced F–O biases under optically thin ice cloud conditions (Figure 7c), but also leads to systematic positive F–O biases for optically thick and multilayered ice clouds (Figures 7e and 7g). Similarly, Grasso et al. (2014) reported that excessive Qc-to-Qg conversion reduces the primary source of anvil ice mass. In contrast to WSM6, the saturation layer in NSSL is positioned at a higher altitude (~250 hPa), accompanied by enhanced concentrations of Qi (~0.034 g kg^{-1}) and Qs (~0.078 g kg^{-1}) extending through the 350–150 hPa layer (Figures 8b and 8d). This elevated saturation level may be conducive to depositional ice growth, which increases the optical depth of ice-phase clouds. As a result, NSSL exhibits reduced F–O biases for optically thick ice clouds, but larger positive biases for optically thin ice clouds (Figures 7d and 7f). This behavior is consistent with previous MPAS- and WRF-model based evaluations showing that NSSL tends to produce larger cloud-ice mass mixing ratios than WSM6 (Chen et al., 2026; Morrison et al., 2015).

During the daytime periods (6–9 h and 30–33 h; 14:00–17:00 SGT), increases in cloud fraction and hydrometeor content in both schemes coincide with reduced warm F–O biases (Figures 7 and 8a-b), indicating enhanced deep convective development that leads to colder simulated BTs closer to the observed values. Conversely, the pronounced reduction in simulated cloud fraction and hydrometeor content during the nighttime periods of 12–18 h and 36–42 h (20:00–02:00 SGT) contributes to larger positive F–Os. Meanwhile, larger STDs as well as reduced predictability, as shown in Figure 7, tend to occur during the nighttime interval of 20:00–05:00 SGT. This period is characterized by enhanced accumulation of Qc in the

https://doi.org/10.5194/egusphere-2026-1476
Preprint. Discussion started: 18 June 2026

mixed-phase layer and decreased cloud fractions, implying an unstable stage of cloud formation or decay. In contrast, smaller STDs during the daytime period of 14:00–17:00 SGT are associated with more fully developed cloud systems, featuring maximized hydrometeor contents (e.g., Qi, Qs, Qg, and Qr) and larger cloud fractions.

Furthermore, the stronger diurnal variability of F–O in NSSL relative to WSM6 under optically thick and multilayered ice cloud conditions (Figure 7) is likely associated with larger-amplitude variations in ice-phase hydrometeors (Qi and Qs) across multiple upper-tropospheric layers, spanning approximately 400–100 hPa (Figures 8b and 8d). During periods of daytime convective activity (14:00–17:00 SGT), enhanced upper-level cloudiness and increased Qi and Qs in NSSL tend to increase ice-cloud optical thickness, leading to colder simulated BTs and larger negative F–O biases (Figures 7f and 7h). At night (20:00–05:00 SGT), the significant decay of ice-phase hydrometeors, together with reduced Qc and Qg contents near the melting layer, decreases the cloud optical thickness markedly, resulting in a shift toward more positive F–O biases (Figures 7f, 7h, 8b, and 8d). By contrast, in WSM6 the larger hydrometeor contents are primarily confined to lower-level Qc and Qg and exhibit relatively weak diurnal variability (Figures 8a and 8c). As a result, their influence on top-of-atmosphere BTs is limited, leading to a comparatively steadier F–O behavior for ice clouds (Figure 7).

https://doi.org/10.5194/egusphere-2026-1476
Preprint. Discussion started: 18 June 2026

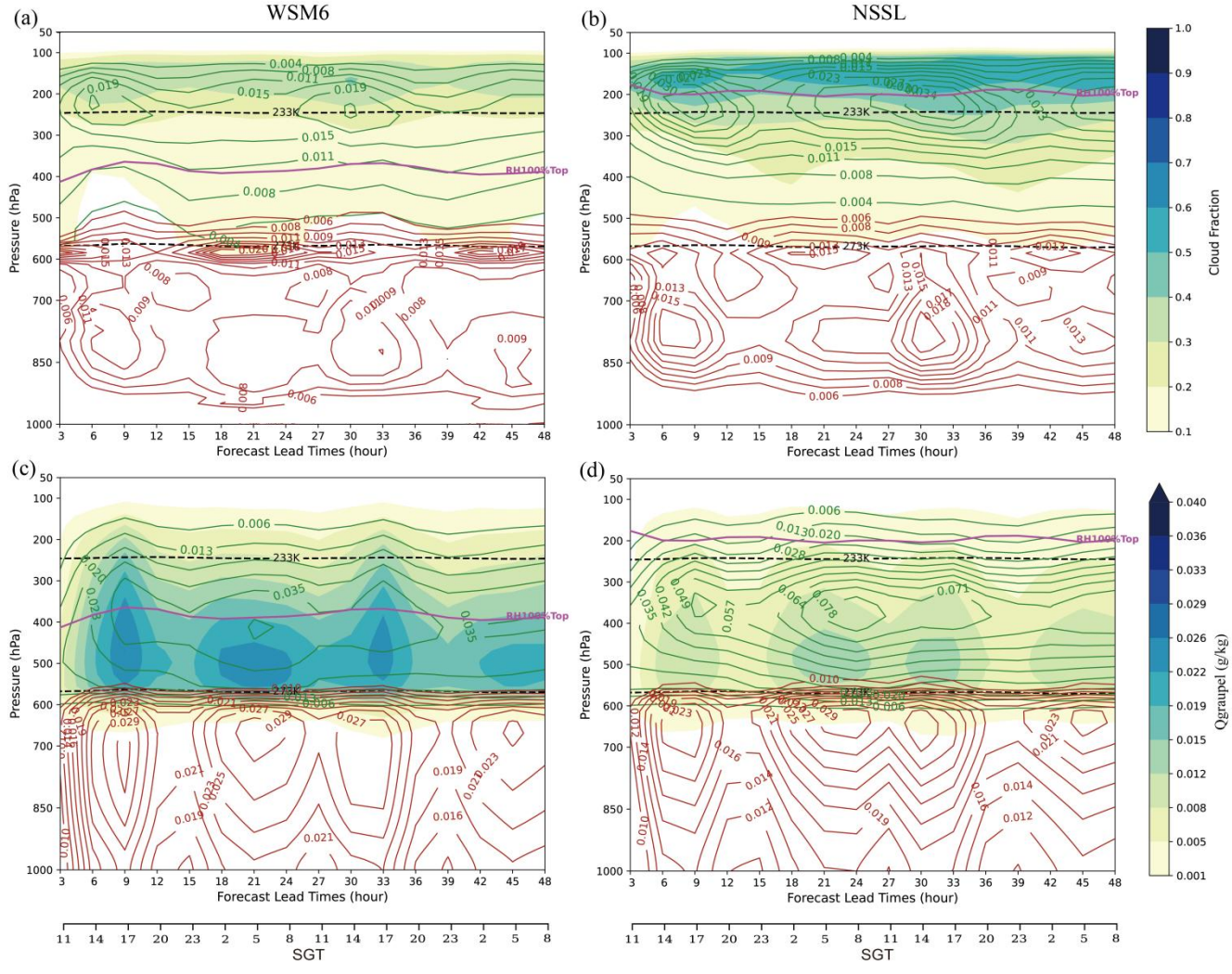

Figure 8. Domain-averaged (a, b) cloud fraction (shading), the mixing ratio (units: g/kg) of Qc (red contours) and Qi (green contours), and (c, d) Qg (shading), Qs (green contours) and Qr (red contours) as a function of forecast lead time and pressure for the WSM6 (first column) and NSSL (second column) microphysics schemes. The dashed black lines mark the 273 K and 233 K isotherms, and the magenta line indicates the uppermost level where the relative humidity reaches 100%.

To evaluate the spatial characteristic of diurnal variations, Figure 9 presents the daytime and nighttime horizontal distributions of F–O BTs for AHI channel 13, averaged within 1° × 1° longitude–latitude bins. During the daytime, both schemes exhibit a distinct land-sea contrast, with predominantly negative F–O biases over land and positive biases over the adjacent oceans. Overall, this land-sea contrast is more pronounced in NSSL, reaching approximately 40–50 K, with cold biases of about -30 K over land and warm biases of roughly 15 K over nearby oceans (Figure 9b). In comparison, WSM6 produces a weaker contrast of roughly 20–40 K, characterized by smaller cold biases over land but stronger warm biases over the ocean (Figure 9a), which are further examined in Figures 10a and 11a. As shown in Figures 9c-d, the negative daytime F–O biases over land shift markedly toward positive values (~5–20 K) at night for both schemes, indicating weakened convection

https://doi.org/10.5194/egusphere-2026-1476
Preprint. Discussion started: 18 June 2026

and reduced cloud amounts after sunset. In particular, over land, the NSSL scheme exhibits a larger diurnal range in F–O (~15–30 K) than WSM6 (~10–25 K). Over the ocean, both schemes show substantially weaker diurnal variability, with NSSL producing more negative F–O biases up to -20 K and WSM6 yielding predominantly positive biases ranging from 10 to 25 K (Figures 9c-d).

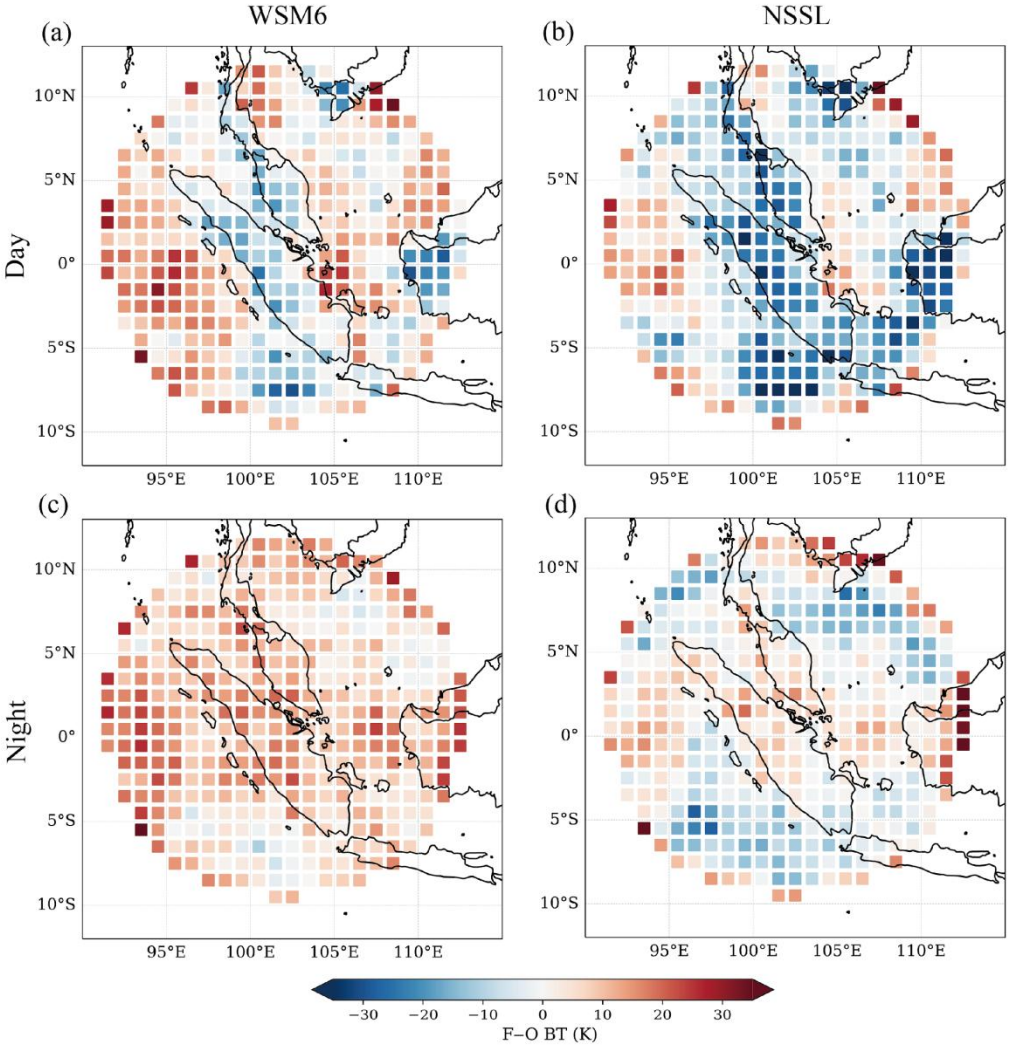

Figure 9. Spatial distributions of the averaged Forecast-Minus-Observation (F–O, units: K) for Himawari-9 channel-13 brightness temperatures, computed within 1° × 1° longitude–latitude bins, during (a, b) the local daytime 11:00-17:00 SGT from a forecast range of 3-9 h and 27-33 h and (c, d) the local nighttime 21:00-03:00 SGT from a forecast range of 13-19 h and 37-43 h for the WSM6 (left) and NSSL (right) schemes.

To further examine the influence of topography and atmospheric environments on cloud diurnal evolution, Figures 10-11 present vertical cross-sections of simulated cloud fraction, vertical velocity, and thermodynamic fields along the S1 and S2 transects shown in Figure 1. The cross-sections across different terrain types reveal that over the mountainous backbone of

https://doi.org/10.5194/egusphere-2026-1476
Preprint. Discussion started: 18 June 2026

central Sumatra (96–101° E), where terrain elevations exceed 1 km, both schemes exhibit enhanced positive potential temperature anomalies during the daytime, accompanied by strong vertical motions and extensive high-cloud coverage between 300 and 100 hPa (Figures 10a–b). This pattern indicates strengthened convective lifting associated with terrain-induced thermodynamic forcing, consistent with previous studies over the Maritime Continent (Coppin et al., 2019; Wei et al., 2022). Notably, NSSL produces stronger vertical velocities extending to higher altitudes, together with thicker high clouds (cloud fraction > 0.7 above ~250 hPa), whereas WSM6 shows relatively shallower updrafts and reduced upper-tropospheric cloud coverage. Meanwhile, both schemes tend to overestimate cloud-top heights over mountainous terrain. These daytime conditions help explain the larger negative F–O biases over land (Figures 9a-b), as orographic enhancement of deep convection along the Barisan Range leads to increased high-level cloud coverage. In contrast, over adjacent seas and coastal lowlands (<1.0 km elevation), weaker potential temperature anomalies and reduced upward motion limit cloud development to below ~400–500 hPa (Figures 10a-b), which is associated with comparatively smaller F–O biases for both schemes (Figures 9a-b).

After sunset, the cross-sectional thermodynamic structure undergoes a distinct phase reversal, as shown in Figures 10c-d. Over the low-elevation plains around 101°–103° E, potential temperature anomalies gradually shift from negative during the day to positive at night, accompanied by predominantly downward motion. Consequently, the convective clouds that develop during the daytime gradually descend and dissipate over these low-lying areas, with more rapid dissipation in WSM6 than in NSSL. This behavior is consistent with the larger positive F–O biases in WSM6 shown in Figures 9c-d. Furthermore, over the high-elevation region (~98°–101° E), even larger positive F–O biases are observed in both schemes relative to the lower-elevation areas (Figures 9c-d), coinciding with a pronounced reduction in cloud amount due to weakened potential temperature anomalies and reduced vertical motion (Figures 10c-d). This feature is likely associated with the diurnal heating–cooling asymmetry over complex terrain. During the daytime, surface warming associated with stronger shortwave solar radiation can occur more rapidly at higher elevations (Pepin et al., 2022), which enhances convective instability and promotes cloud development (Hartmann et al., 2018). In contrast, greater attenuation of solar radiation over lower terrain, owing to a higher atmospheric extinction rate associated with airmass, water vapor, and aerosols, may limit surface heating and suppress convection (Yang et al., 2010). At night, longwave radiative cooling combined with weaker vertical motion over elevated terrain is likely to stabilize the boundary layer and inhibit convective activity (Sokol et al., 2020). Meanwhile, over the low-lying plains (~101°–103° E), downslope valley flows may promote moisture convergence and low-level cloud development (Figures 10c-d).

https://doi.org/10.5194/egusphere-2026-1476
Preprint. Discussion started: 18 June 2026

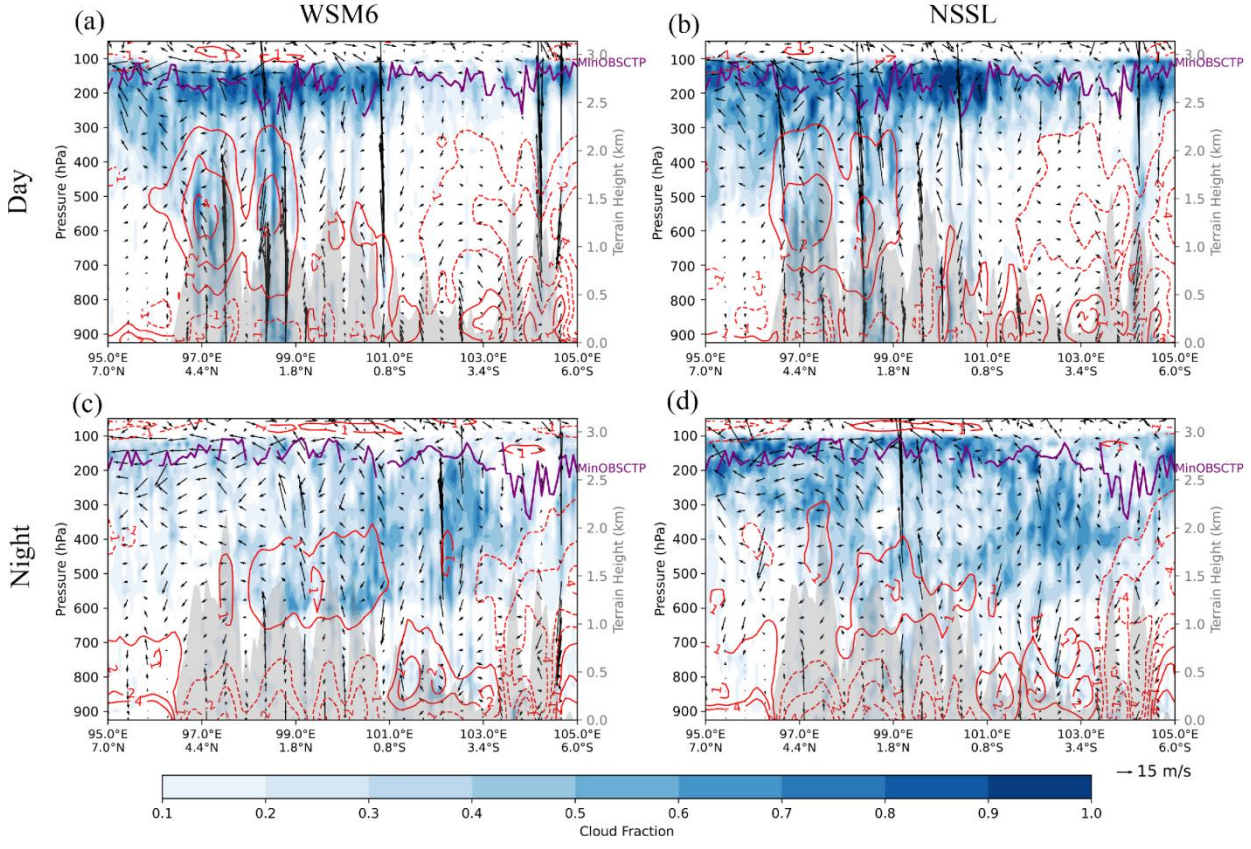

Figure 10. Mean cross-sections of the cloud fraction (blue-filled contours), vertical velocity (black vectors; units: m/s), equivalent potential temperature anomaly (red contours; units: K), minimum observed cloud-top pressures (purple lines; units: hPa) and terrain height (grey shading; units: km) along the S1 transect shown in Figure 1 for the (a, b) 11:00-17:00 SGT daytime from a forecast range of 3-9 h and 27-33 h and (c, d) 21:00-03:00 SGT nighttime from the 13-19 h and 37-43 h forecasts in WSM6 (first column) and NSSL (second column) experiments.

Along the S2 transect, as illustrated in Figures 11a-b, the daytime-minus-nighttime differences in near-surface temperature (T2 m) and specific humidity (Q2 m) reveal a pronounced land–sea thermodynamic contrast extending from the eastern Indian Ocean to western Java. Over the ocean (~99–100° E and ~101.8–102.5° E), T2 m remains nearly constant at around 301 K, whereas inland temperatures near 100.4° E and 101.8° E increase from nighttime to daytime by approximately 2–8 K in both schemes (red curves in Figures 11a-b), reflecting enhanced daytime shortwave heating and nighttime longwave radiative cooling over land. Meanwhile, the daytime-minus-nighttime difference in Q2 m shows an increase of about 1–3 g kg^{-1} from the ocean toward inland regions (blue curves in Figures 11a-b). This enhanced land–sea thermodynamic gradient appears to strengthen vertical motion along the coastal interface and promote convective development extending to above ~200 hPa (Figures 11c-f). In contrast to the pronounced land-based diurnal variability, the adjacent coastal oceans maintain relatively stable thermodynamic conditions, primarily due to the greater heat capacity and thermal inertia of seawater compared with land.

https://doi.org/10.5194/egusphere-2026-1476
Preprint. Discussion started: 18 June 2026

Therefore, the amplified land–sea thermodynamic contrast appears to facilitate vigorous cloud evolution over land and adjacent coastal regions, with cloud fractions frequently exceeding 0.7 between 100 and 300 hPa during the daytime (Figures 11c-d), followed by rapid nocturnal subsidence and dissipation to below ~300 hPa (Figures 11e-f). Consequently, the deeper and higher clouds developing over land during the daytime are associated with more negative F–O biases (Figures 9a-b), as increased cloud optical thickness elevates the effective infrared radiating level to colder cloud tops, resulting in lower simulated BTs. Likewise, rapid cloud dissipation over land at night corresponds to pronounced positive F–O biases. Over the ocean, the relatively stable near-surface thermodynamic environment, together with weaker convective instability, maintains cloud fractions at more steady levels (~0.3–0.6) above ~400 hPa during both daytime and nighttime. This may explain the persistence of some negative F–O biases over the ocean within 102.0–102.5° E and 6.0–9.0° N throughout the diurnal cycle (Figure 9). Furthermore, compared with WSM6, the larger diurnal F–O amplitude produced by NSSL over land (Figures 9b and 9d) is likely related to its simulation of stronger upper-tropospheric vertical motion around 100-300 hPa (Figures 10 and 11), which may enhance the diurnal evolution of Qi and Qs in high-level clouds through lofting and sedimentation processes.

https://doi.org/10.5194/egusphere-2026-1476
Preprint. Discussion started: 18 June 2026

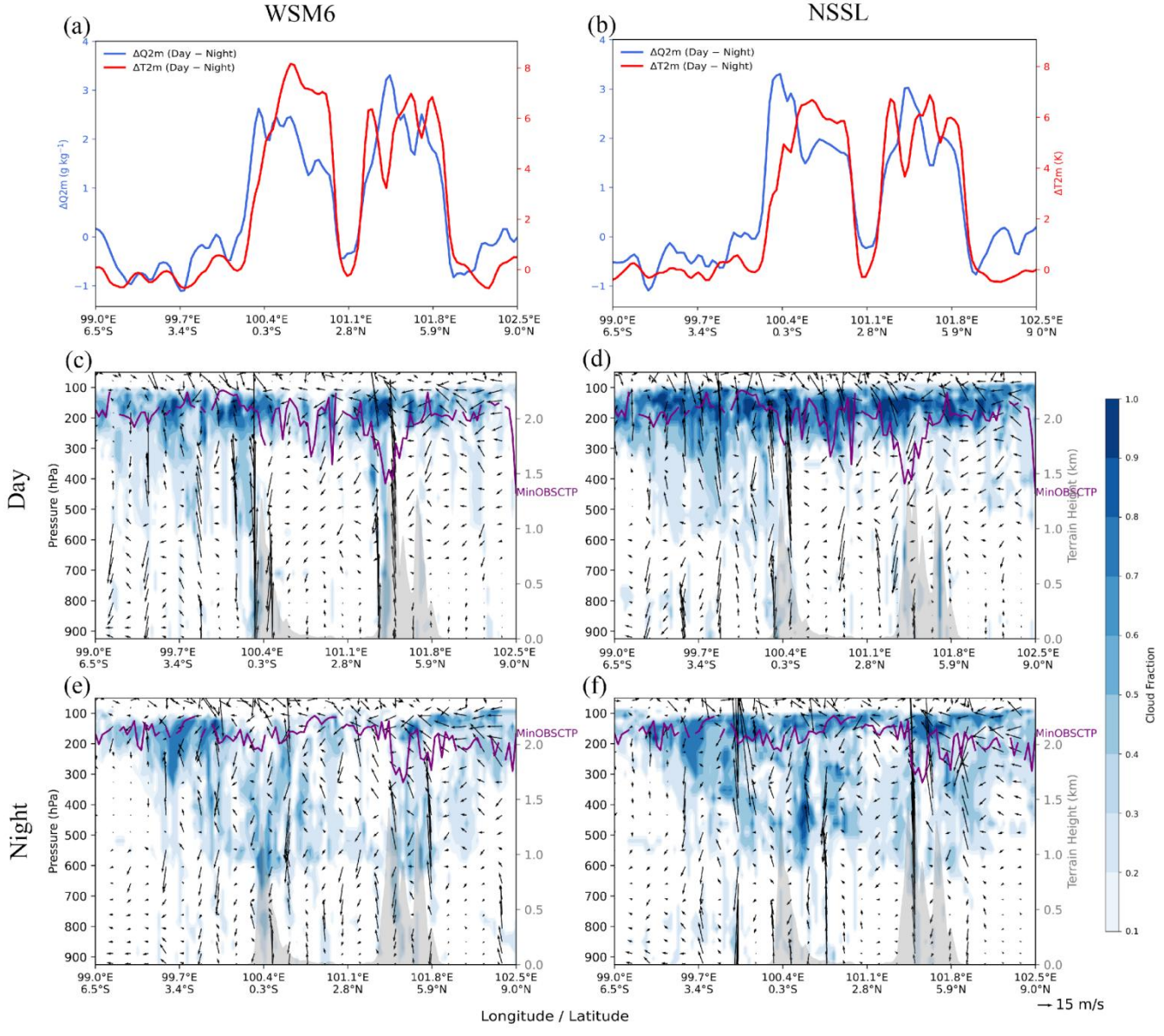

Figure 11. Vertical cross-sections of daytime-minus-nighttime differences in (a, b) 2 m specific humidity (blue lines; units: g kg^{-1}) and 2 m temperature (red lines; units: K) along the S2 transect shown in Figure 1, together with simulated cloud fraction (blue-filled contours), vertical velocity (black vectors; units: m s^{-1}), ,minimum AHI L2 cloud-top pressure (purple contours; units: hPa), and terrain height (grey shading; units: km) during (c, d) 11:00-17:00 SGT daytime from a forecast range of 3-9 h and 27-33 h and (e, f) 21:00-03:00 SGT nighttime from the 13-19 h and 37-43 h forecasts simulated by the WSM6 (first column) and NSSL (second column) microphysics schemes.

4 Summary

Tropical cloud prediction over the Maritime Continent remains a persistent challenge for numerical weather prediction models, as forecast performance is strongly constrained by uncertainties in microphysical parameterizations under complex terrain and

https://doi.org/10.5194/egusphere-2026-1476
Preprint. Discussion started: 18 June 2026

atmospheric conditions. To support model development for cloud prediction over this region, Himawari-9 AHI multi-band radiances together with Level-2 cloud products are jointly used to evaluate the tropical cloud characteristics simulated by MPAS using the WSM6 and NSSL microphysics schemes. The proposed infrared-radiance-based framework is further designed to exploit these high-resolution satellite observations more effectively for model assessment. The main findings are summarized below.

The evaluation using multi-band AHI radiance data shows that WSM6 more accurately represents the observed BT range in the water-vapor bands, whereas NSSL yields a more realistic simulation of window-channel BTs. Night-time diagnostics for channel 7 (3.9 μm) further suggest that BTs associated with low-level clouds and fog are simulated more realistically in NSSL than in WSM6.

The cloud-amount evaluation with AHI cloud mask retrievals suggests that NSSL achieves higher skill in representing overall cloudiness, particularly in the spatial placement of cloudy pixels. However, the WSM6 simulations exhibit larger spatial displacement errors and tend to overestimate cloud fraction by misclassifying clear-sky pixels as cloudy during the model spin-up period. In terms of vertical cloud structure, relative to AHI cloud-top observations, both schemes tend to overpredict cloud-top heights for high-level clouds, while underpredicting mid- and low-level clouds. A comparable cloud-height bias has been reported in WRF microphysics evaluations, where cloud-top heights are generally overestimated, potentially linked to an overabundance of upper-level cloud ice (Zhu et al., 2023), whereas mid-level cloudiness appears to be underestimated (Jankov et al., 2011).

The AHI cloud-type diagnostics further indicate that WSM6 tends to underpredict the frequency of optically thick ice clouds, leading to systematic warm biases in F–O. This tendency is consistent with previous findings that suggest an underrepresentation of upper-level ice clouds in WSM6 (Grasso et al., 2014). These biases are likely associated with limited development of upper-level solid-phase hydrometeors under weaker upper-tropospheric updrafts and lower saturation levels. In contrast, NSSL produces more abundant ice and snow hydrometeors above ~500 hPa within higher saturation layers and stronger upper-level ascent, resulting in smaller F–O for optically thick ice clouds. However, NSSL tends to underpredict the frequency of thin ice clouds and exhibits larger positive F–O biases than WSM6 in these regimes. Despite these differences, both schemes exhibit relatively higher predictive skill for liquid-water and optically thin ice clouds than for other cloud types. In contrast, multilayer ice clouds are associated with the largest forecast errors in both schemes, particularly in NSSL, where larger F–O biases and standard deviations are evident.

Moreover, both schemes exhibit clear cloud-related diurnal variations in F–O, especially over land, with negative daytime departures suggesting an overestimation of cloud-top height and/or high-cloud amount. At night, F – O departures shift to positive values, likely reflecting an underestimation of high-level or optically thick clouds. This behavior is likely driven by diurnal heating – cooling asymmetry over complex terrain associated with surface radiative forcing. The land – sea thermodynamic contrast may further enhance cloud development over land and adjacent coastal regions. Based on Himawari-8 AHI observations over East Asia and the Tibetan Plateau, Chen et al. (2018) likewise found that the diurnal amplitude of cloudiness is larger over land than over ocean and tends to increase over complex terrain. Compared with WSM6, the larger

https://doi.org/10.5194/egusphere-2026-1476
Preprint. Discussion started: 18 June 2026

diurnal F–O amplitude in NSSL is consistent with its more pronounced diurnal variability in upper-tropospheric ice-phase hydrometeors, which may be related to stronger upper-level ascent and higher supersaturation layers.

The above findings highlight several directions for future development in both model forecasting and all-sky infrared radiance assimilation. On the modelling side, improving the representation of ice-phase hydrometeor partitioning is essential for better distinguishing among optically thick, thin, and multilayer ice clouds. In addition, more accurate simulation of upper-tropospheric dynamical and thermodynamic conditions (e.g., upper-level winds, supersaturation, and vertical transport of condensate) is crucial for reducing cloud-top height biases. Over the Maritime Continent, improved representations of land-surface meteorological processes and terrain effects may further improve the simulation of tropical cloud diurnal evolution. From the data assimilation perspective, applying cloud-type-dependent bias correction or quality-control strategies within the all-sky infrared assimilation framework may improve performance under specific cloud regimes. Future all-sky assimilation experiments would also benefit from incorporating diurnally varying hydrometeor background-error structures to better capture pronounced day–night contrasts. Moreover, targeted observing-system experiments that select infrared channels according to cloud-regime sensitivities and microphysics-scheme-dependent simulation characteristics may help optimize the use of Himawari-9 radiances in tropical cloud assimilation. Despite the insights gained from the present experiments, several limitations remain. The current results are based on a limited number of cases and time periods, and their robustness would benefit from evaluation using longer time series and a broader range of weather systems. In addition, future studies could incorporate additional observational datasets, such as radar and microwave measurements, to enable a more comprehensive assessment of sub-cloud and in-cloud microphysical properties.

Code and Data Availability

The source code of MPAS-JEDI version 3.0.3 is archived on Zenodo at https://doi.org/10.5281/zenodo.19209009 (last access: 10 June 2026; JCSDA and NCAR, 2025). The MPAS-Atmosphere version 8.2.2 and the CRTM version 2.4.1 are also available via Zenodo at https://doi.org/10.5281/zenodo.13821326 (last access: 10 June 2026; Duda et al. 2024) and https://doi.org/10.5281/zenodo.7823722 (last access: 10 June 2026; Johnson et al., 2023), respectively. All model configuration files, data processing codes, and auxiliary scripts required to reproduce the results of this study are publicly available on Zenodo at https://doi.org/10.5281/zenodo.19925596 (last access: 10 June 2026; Zhang et al., 2026a). The ECMWF HRES data, provided by the Centre for Climate Research Singapore (CCRS) under the NCAR–CCRS collaborative project, are subject to third-party access and redistribution restrictions, and access requests should be directed by email to the corresponding author. The processed Himawari-9 AHI observation data used in this study have been archived on Zenodo at https://doi.org/10.5281/zenodo.20312122 (last access: 10 June 2026; Zhang et al., 2026b). The model output data are available from the corresponding author upon request due to their large volume.

https://doi.org/10.5194/egusphere-2026-1476
Preprint. Discussion started: 18 June 2026

Author contributions

X.Z. and L.J. developed the verification methods. X.Z. conducted the experiments, performed the testing and validation, and prepared the manuscript. L.J. and Z.L. contributed to additional testing and validation of the datasets and results. Z.L. also provided valuable feedback on the development and implementation of the verification procedures, as well as on the manuscript. T.S., W.W., and I.-H.C. provided technical assistance and offered scientific suggestions that helped improve the study. All authors have read and agreed to the published version of the manuscript.

Competing interests

The contact author has declared that none of the authors has any competing interests.

Disclaimer

Publisher's note: Copernicus Publications remains neutral with regard to jurisdictional claims made in the text, published maps, institutional affiliations, or any other geographical representation in this paper. While Copernicus Publications makes every effort to include appropriate place names, the final responsibility lies with the authors. Views expressed in the text are those of the authors and do not necessarily reflect the views of the publisher.

Acknowledgements

The authors gratefully acknowledge the SINGV-NG team from both the National Center for Atmospheric Research and the Centre for Climate Research Singapore (CCRS) for their dedicated collaboration in the development of the system. We also acknowledge the Computational and Information Systems Laboratory (CISL) at NSF National Center for Atmospheric Research (NCAR) for their technical support.

Financial support

This research was supported by the Centre for Climate Research Singapore (CCRS) of the Meteorological Service Singapore.

References

Aslam, A. A.: Rainfall over the Maritime Continent: key processes, scale interactions and model representation. Weather, 80, 176–185, https://doi.org/10.1002/wea.7731, 2025.

https://doi.org/10.5194/egusphere-2026-1476
Preprint. Discussion started: 18 June 2026

Atlas, R. L., Bretherton, C. S., Sokol, A. B., Blossey, P. N., and Khairoutdinov, M. F.: Tropical cirrus are highly sensitive to ice microphysics within a nudged global storm-resolving model, *Geophys. Res. Lett.*, 51, e2023GL105868, https://doi.org/10.1029/2023GL105868, 2024.

Aumann, H. H., Chen, X., Fishbein, E., Geer, A., Havemann, S., Huang, X., and Coauthors: Evaluation of radiative transfer models with clouds, *J. Geophys. Res. Atmos.*, 123, 6142–6157, https://doi.org/10.1029/2017JD028063, 2018.

Battaglia, A., Kollias, P., Dhillon, R., Roy, R., Tanelli, S., Lamer, K., and Coauthors: Spaceborne cloud and precipitation radars: Status, challenges, and ways forward, *Rev. Geophys.*, 58, e2019RG000686, https://doi.org/10.1029/2019RG000686, 2020.

Bessho, K., and Coauthors: An introduction to Himawari-8/9—Japan's new-generation geostationary meteorological satellites, *J. Meteor. Soc. Japan*, 94, 151–183, https://doi.org/10.2151/jmsj.2016-009, 2016.

Centurioni, L. R., and Coauthors: Global in situ observations of essential climate and ocean variables at the air–sea interface, *Front. Mar. Sci.*, 6, 419, https://doi.org/10.3389/fmars.2019.00419, 2019.

Chang, C., Lu, M., and Lim, H.: Monsoon convection in the Maritime Continent: Interaction of large-scale motion and complex terrain, *Meteor. Monogr.*, 56, 6.1–6.29, https://doi.org/10.1175/AMSMONOGRAPHS-D-15-0011.1, 2016.

Chen, D., Guo, J., Wang, H., Li, J., Min, M., Zhao, W., and Yao, D.: The cloud top distribution and diurnal variation of clouds over East Asia: preliminary results from Advanced Himawari Imager, *J. Geophys. Res. Atmos.*, 123, 3724 – 3739, https://doi.org/10.1002/2017JD028044, 2018.

Chen, I.-H., Patel, P., Furtado, K., Wang, W., Liu, Z., Barker, D., Dudhia, J., Zhang, H.: Performance evaluation of regional weather predictions with the Model for Prediction Across Scales – Atmosphere (MPAS-A) over the Maritime Continent. *Q. J. R. Meteorol. Soc*, e70129, https://doi.org/10.1002/qj.70129, 2026.

Chen, Y., Weng, F., Han, Y., and Liu, Q.: Validation of the community radiative transfer model using CloudSat data, *J. Geophys. Res.*, 113, D00A03, https://doi.org/10.1029/2007JD009561, 2008.

Cho, H., Jun, S. Y., Ho, C. H., and McFarquhar, G.: Simulations of winter Arctic clouds and associated radiation fluxes using different cloud microphysics schemes in the Polar WRF: Comparisons with CloudSat, CALIPSO, and CERES, *J. Geophys. Res. Atmos.*, 125, https://doi.org/10.1029/2019JD031413, 2020.

Chow, W. T. L., Cheong, B. D., and Ho, B. H.: A multimethod approach towards assessing urban flood patterns and its associated vulnerabilities in Singapore, *Adv. Meteorol.*, 2016, 7159132, https://doi.org/10.1155/2016/7159132, 2016.

Cintineo, R., Otkin, J., Xue, M., and Kong, F.: Evaluating the performance of planetary boundary layer and cloud microphysical parameterization schemes in convection-permitting ensemble forecasts using synthetic GOES-13 satellite observations, *Mon. Weather Rev.*, 142, 163–182, https://doi.org/10.1175/MWR-D-13-00143.1, 2014.

Comin, A. N., Schumacher, V., Justino, F., and Fernández, A.: Impact of different microphysical parameterizations on extreme snowfall events in the southern Andes, *Wea. Climate Extremes*, 21, 65–75, https://doi.org/10.1016/j.wace.2018.07.001, 2018.

https://doi.org/10.5194/egusphere-2026-1476
Preprint. Discussion started: 18 June 2026

Coppin, D., and Bellon, G.: Physical mechanisms controlling the offshore propagation of convection in the tropics: 2. Influence of topography, *J. Adv. Model. Earth Syst.*, 11, 3251–3264, https://doi.org/10.1029/2019MS001794, 2019.

Dawson, D. T., Xue, M., Milbrandt, J. A., and Yau, M. K.: Comparison of evaporation and cold pool development between single-moment and multimoment bulk microphysics schemes in idealized simulations of tornadic thunderstorms, *Mon. Weather Rev.*, 138, 1152–1171, https://doi.org/10.1175/2009MWR2956.1, 2010.

Dipankar, A., Webster, S., Sun, X., and Coauthors: SINGV: A convective-scale weather forecast model for Singapore, *Q. J. R. Meteorol. Soc.*, 146, 4131–4146, https://doi.org/10.1002/qj.3895, 2020.

Duda, M., Jacobsen, D., Petersen, M., Hoffman, M., ldfowler58, Turner, A. K., Asay-Davis, X., Ringler, T., Roekel, L. V., Curry, M., Lipscomb, W., stephenprice, skamaroc, Jeffery, N., Heinzeller, D., Woodring, J., Wolfram, P. J., Dickerson, G. D., maltrud, Saenz, J. Nick, weiwangncar, Mametjanov, A., mperego, Werner, K., Wolfe, J., W, J., Jones, P., Werner, K., and Larofeticus: MPAS-Dev/MPAS-Model: MPAS Version 8.2.2 (v8.2.2), Zenodo [code], https://doi.org/10.5281/zenodo.13821326, 2024.

ECMWF: IFS documentation – CY49R1, Part I: Observations, European Centre for Medium-Range Weather Forecasts, Reading, UK, available at: https://www.ecmwf.int/en/publications/ifs-documentation, 2024.

ECMWF: Medium cloud parameters, available at: https://charts.ecmwf.int/products/medium-cloud-parameters (accessed 2025).

ECMWF: Medium cloud parameters, available at: https://charts.ecmwf.int/products/medium-cloud-parameters (accessed 2025).

Feofilov, A. G., and Stubenrauch, C. J.: Diurnal variation of high-level clouds from the synergy of AIRS and IASI space-borne infrared sounders, *Atmos. Chem. Phys.*, 19, 13957–13972, https://doi.org/10.5194/acp-19-13957-2019, 2019.

Ferrier, B.: A double-moment multiple-phase four-class bulk ice scheme. Part I: Description, *J. Atmos. Sci.*, 51, 249–280, https://doi.org/10.1175/1520-0469(1994)051<0249:ADMMPF>2.0.CO;2, 1994.

Franklin, C. N., Sun, Z., Bi, D., Dix, M., Yan, H., and Bodas Salcedo, A.: Evaluation of clouds in ACCESS using the satellite simulator package COSP: Global, seasonal, and regional cloud properties, *J. Geophys. Res. Atmos.*, 118, 732–748, https://doi.org/10.1029/2012JD018469, 2013.

Galligani, V. S., Wang, D., Alvarez Imaz, M., Salio, P., and Prigent, C.: Analysis and evaluation of WRF microphysical schemes for deep moist convection over south-eastern South America (SESA) using microwave satellite observations and radiative transfer simulations, *Atmos. Meas. Tech.*, 10, 3627–3649, https://doi.org/10.5194/amt-10-3627-2017, 2017.

Gehne, M., Wolding, B., Dias, J., and Kiladis, G. N.: Diagnostics of tropical variability for numerical weather forecasts, *Wea. Forecasting*, 37, 1661–1680, https://doi.org/10.1175/WAF-D-21-0204.1, 2022.

Geiss, S., Scheck, L., de Lozar, A., and Weissmann, M.: Understanding the model representation of clouds based on visible and infrared satellite observations, *Atmos. Chem. Phys.*, 21, 12273–12290, https://doi.org/10.5194/acp-21-12273-2021, 2021.

https://doi.org/10.5194/egusphere-2026-1476
Preprint. Discussion started: 18 June 2026

Gevorgyan, A.: Convection-permitting simulation of a heavy rainfall event in Armenia using the WRF model, *J. Geophys. Res. Atmos.*, 123, 11008–11029, https://doi.org/10.1029/2017JD028247, 2018.

Grasso, L., Lindsey, D. T., Lim, K.-S. S., Clark, A., Bikos, D., and Dembek, S. R.: Evaluation of and suggested improvements to the WSM6 microphysics in WRF-ARW using synthetic and observed GOES-13 imagery, *Mon. Weather Rev.*, 142, 3635–3650, https://doi.org/10.1175/MWR-D-14-00005.1, 2014.

Grecu, M., and Krajewski, W. F.: A large-sample investigation of statistical procedures for radar-based short-term quantitative precipitation forecasting, *J. Hydrol.*, 239, 69–84, https://doi.org/10.1016/S0022-1694(00)00360-7, 2000.

Griffin, S. M., and Otkin, J. A.: Evaluating the impact of planetary boundary layer, land surface model, and microphysics parameterization schemes on simulated GOES-16 water vapor brightness temperatures, *Atmosphere*, 13, 366, https://doi.org/10.3390/atmos13030366, 2022.

Griffin, S. M., Otkin, J. A., Rozoff, C. M., Sieglaff, J. M., Cronce, L. M., and Alexander, C. R.: Methods for comparing simulated and observed satellite infrared brightness temperatures and what do they tell us?, *Wea. Forecasting*, 32, 5–25, https://doi.org/10.1175/WAF-D-16-0098.1, 2017a.

Griffin, S. M., Otkin, J. A., Rozoff, C. M., Sieglaff, J. M., Cronce, L. M., Alexander, C. R., Jensen, T. L., and Wolff, J. K.: Seasonal analysis of cloud objects in the High Resolution Rapid Refresh (HRRR) model using object-based verification, *J. Appl. Meteor. Climatol.*, 56, 2317–2334, https://doi.org/10.1175/JAMC-D-17-0004.1, 2017b.

Guo, B., Zhang, F., Zhao, Z., Guo, J., and Li, W.: Retrieval of cloud macro-physical properties using the FY-4A advanced geostationary radiation imager (AGRI) and the geostationary interferometric infrared sounder (GIIRS), *Geophys. Res. Lett.*, 51, e2024GL109772, https://doi.org/10.1029/2024GL109772, 2024.

Guerrette, J. J., Liu, Z., Snyder, C., Jung, B.-J., Schwartz, C. S., Ban, J., Vahl, S., Wu, Y., Baños, I. H., Yu, Y. G., Ha, S., Trémolet, Y., Auligné, T., Gas, C., Ménétrier, B., Shlyaeva, A., Miesch, M., Herbener, S., Liu, E., Holdaway, D., and Johnson, B. T.: Data assimilation for the Model for Prediction Across Scales–Atmosphere with the Joint Effort for Data Assimilation Integration (JEDI–MPAS 2.0.0-beta): Ensemble of En-3DEnVar assimilations, *Geosci. Model Dev.*, 16, 7123–7142, https://doi.org/10.5194/gmd-16-7123-2023, 2023.

Hartmann, B., Gasparini, B., Berry, S. E., and Blossey, P. N.: The life cycle and net radiative effect of tropical anvil clouds, *J. Adv. Model. Earth Syst.*, 10, 3012–3029, https://doi.org/10.1029/2018MS001484, 2018.

Hashino, T., Satoh, M., Hagihara, Y., Kubota, T., Matsui, T., Nasuno, T., and Okamoto, H.: Evaluating cloud microphysics from NICAM against CloudSat and CALIPSO, *J. Geophys. Res. Atmos.*, 118, 7273–7292, https://doi.org/10.1002/jgrd.50564, 2013.

Haynes, J. M., Noh, Y., Miller, S. D., Haynes, K. D., Ebert-Uphoff, I., and Heidinger, A.: Low cloud detection in multilayer scenes using satellite imagery with machine learning methods, *J. Atmos. Oceanic Technol.*, 39, 319–334, https://doi.org/10.1175/JTECH-D-21-0084.1, 2022.

https://doi.org/10.5194/egusphere-2026-1476
Preprint. Discussion started: 18 June 2026

Heidinger, A., Li, Y., and Wanzong, S.: NOAA AWG cloud height algorithm (ACHA), version 3.4, Algorithm Theoretical Basis Document, *NOAA NESDIS Center for Satellite Applications and Research*, 89 pp., https://www.star.nesdis.noaa.gov/jpss/documents/ATBD/ATBD_EPS_Cloud_ACHA_v3.4.pdf, 2018.

Heidinger, A., and Straka, W.: NOAA Enterprise Cloud Mask (ECM), version 1.2, Algorithm Theoretical Basis Document, *NOAA NESDIS Center for Satellite Applications and Research*, 77 pp.,https://www.star.nesdis.noaa.gov/goesr/documents/ATBDs/Enterprise/ATBD_Enterprise_Cloud_Mask_v1.2_2020_10_01.pdf, 2020.

Heidinger, A. K.: ABI cloud height, Algorithm Theoretical Basis Document, *NOAA NESDIS Center for Satellite Applications and Research*, 77 pp., https://www.star.nesdis.noaa.gov/goesr/documents/ATBDs/Baseline/ATBD_GOES-R_Cloud_Height_v3.0_Jul2012.pdf, 2012.

Hong, S., Dudhia, J., and Chen, S.: A revised approach to ice microphysical processes for the bulk parameterization of clouds and precipitation, *Mon. Weather Rev.*, 132, 103–120, https://doi.org/10.1175/1520-0493(2004)132<0103:ARATIM>2.0.CO;2, 2004.

Hong, S.-Y., and Lim, J.-O. J.: The WRF single-moment 6-class microphysics scheme (WSM6), *J. Korean Meteor. Soc.*, 42, 129–151, https://www2.mmm.ucar.edu/wrf/users/workshops/WS2006/abstracts/PSession05/P5_4_Hong.pdf, 2006.

Huang, Y., Siems, S., Manton, M., Protat, A., Majewski, L., and Nguyen, H.: Evaluating Himawari-8 cloud products using shipborne and CALIPSO observations: Cloud-top height and cloud-top temperature, *J. Atmos. Oceanic Technol.*, 36, 2327–2347, https://doi.org/10.1175/JTECH-D-18-0231.1, 2019.

Huang, Y., Wang, Y., Xue, L., and Li, H.: Comparison of three microphysics parameterization schemes in the WRF model for an extreme rainfall event in the coastal metropolitan city of Guangzhou, *China, Atmos. Res.*, 246, 105105, https://doi.org/10.1016/j.atmosres.2020.104939, 2020.

Huang, Y., Liu, Y., Liu, Y., and Knievel, J. C.: Mechanisms for a record-breaking rainfall in the coastal metropolitan city of Guangzhou, China: Observation analysis and nested very large eddy simulation with the WRF model, *J. Geophys. Res. Atmos.*, 124, 1370–1391, https://doi.org/10.1029/2018JD029668, 2019a.

Huang, Y., Liu, Y., Liu, Y., and Knievel, J. C.: Budget analyses of a record-breaking rainfall event in the coastal metropolitan city of Guangzhou, China, *J. Geophys. Res. Atmos.*, https://doi.org/10.1029/2018JD030229, 2019b.

Huo, J., Bi, Y., Wang, H., Zhang, Z., Song, Q., Duan, M., and Han, C.: A comparative study of cloud microphysics schemes in simulating a quasi-linear convective thunderstorm case, *Remote Sens.*, 16, 3259, https://doi.org/10.3390/rs16173259, 2024.

Igel, A. L., van den Heever, S. C., and Johnson, J. S.: Make it a double? Sobering results from simulations using single-moment microphysics schemes, *J. Atmos. Sci.*, 72, 910–925, https://doi.org/10.1175/JAS-D-14-0107.1, 2015.

Imai, T., and Yoshida, R.: Algorithm theoretical basis for Himawari-8 cloud mask product, Meteorological Satellite Center Technical Note No. 61, *Japan Meteorological Agency*, 17 pp., https://www.data.jma.go.jp/mscweb/technotes/msctechrep61-1.pdf, 2016.

https://doi.org/10.5194/egusphere-2026-1476
Preprint. Discussion started: 18 June 2026

Iwabuchi, H., Saito, M., Tokoro, Y., and Coauthors: Retrieval of radiative and microphysical properties of clouds from multispectral infrared measurements, *Prog. in Earth and Planet. Sci*., 3, 32, https://doi.org/10.1186/s40645-016-0108-3, 2016.

Jankov, I., Grasso, L. D., Sengupta, M., Neiman, P. J., Zupanski, D., Zupanski, M., Lindsey, D., Hillger, D. W., Birkenheuer, D. L., Brummer, R., and Yuan, H.: An evaluation of five ARW-WRF microphysics schemes using synthetic GOES imagery for an atmospheric river event affecting the California coast, *J. Hydrometeorol.*, 12, 618–633, doi:10.1175/2010JHM1282.1, 2011.

Jin, D., Oreopoulos, L., Lee, D., Cho, N., and Tan, J.: Contrasting the co-variability of daytime cloud and precipitation over tropical land and ocean, *Atmos. Chem. Phys.*, 18, 3065–3082, https://doi.org/10.5194/acp-18-3065-2018, 2018.

Johnson, B. T., Dang, C., Stegmann, P., Liu, Q., Moradi, I., and Auligné, T.: The Community Radiative Transfer Model (CRTM): Community-focused collaborative model development accelerating research to operations, *Bull. Amer. Meteor. Soc.*, 104, E1817–E1830, https://doi.org/10.1175/BAMS-D-22-0015.1, 2023.

Johnson, B. T., Hocking, J., and Rundle, D.: Comparison of RTTOV and CRTM in JEDI, Visiting Scientist Report NWPSAF-MO_VS-060, version 1.0, *EUMETSAT NWP SAF / JCSDA / Met Office*, 14 pp., https://nwp-saf.eumetsat.int/publications/vs_reports/nwpsaf-mo-vs-060.pdf, 2023.

Johnson, B. T., Dang, C., Rosinski, J., YingtaoMa, StegmannJCSDA and Kasprzyk, P.:JCSDA/crtm: v2.4.1-jedi public release for UFO/JEDI (v2.4.1-jedi), Zenodo [code], https://doi.org/10.5281/zenodo.7823722, 2023.

Joint Center for Satellite Data Assimilation and National Center for Atmospheric Research: JEDI-MPAS Data Assimilation System v3.0.3 (3.0.3), Zenodo [code], https://doi.org/10.5281/zenodo.19209009, 2025.

Jones, T. A., Otkin, J. A., Stensrud, D. J., and Knopfmeier, K.: Assimilation of satellite infrared radiances and Doppler radar observations during a cool season observing system simulation experiment, *Mon. Weather Rev.*, 141, 3273–3299, https://doi.org/10.1175/MWR-D-12-00267.1, 2013.

Jones, T. A., Skinner, P., Knopfmeier, K., Mansell, E., Minnis, P., Palikonda, R., and Smith, W.: Comparison of cloud microphysics schemes in a Warn-on-Forecast system using synthetic satellite objects, *Wea. Forecasting*, 33, 1681–1708, https://doi.org/10.1175/WAF-D-18-0112.1, 2018.

Kanase, R. D., and Salvekar, P. S.: Impact of physical parameterization schemes on track and intensity of severe cyclonic storms in the Bay of Bengal, *Meteorol. Atmos. Phys.*, 127, 537–559, https://doi.org/10.1007/s00703-015-0381-5, 2015.

Khain, A. P., Beheng, K. D., Heymsfield, A., Korolev, A., Krichak, S. O., Levin, Z., Pinsky, M., Phillips, V., Prabhakaran, T., Teller, A., and Coauthors: Representation of microphysical processes in cloud-resolving models: Spectral (bin) microphysics versus bulk parameterization, *Rev. Geophys.*, 53, 247–322, https://doi.org/10.1002/2014RG000468, 2015.

Kim, Y.-S., Wang, X., and Johnson, A.: Impact of microphysics parameterization schemes on the assimilation of GOES-16 ABI all-sky infrared radiances for a bow echo analysis and prediction, *J. Geophys. Res. Atmos.*, 129, e2023JD040046, https://doi.org/10.1029/2023JD040046, 2024.

https://doi.org/10.5194/egusphere-2026-1476
Preprint. Discussion started: 18 June 2026

Köcher, G., Zinner, T., and Knote, C.: Influence of cloud microphysics schemes on weather model predictions of heavy precipitation, *Atmos. Chem. Phys.*, 23, 6255–6269, https://doi.org/10.5194/acp-23-6255-2023, 2023.

Lee, J. C. K., Zhang, H., Barker, D. M., Chen, S., Kumar, R., An, B. W., Sharma, K., and Stephens-Chandramouli, K.: Weather prediction for Singapore—Progress, challenges, and opportunities, *Meteorology*, 1, 394–401, https://doi.org/10.3390/meteorology1040025, 2022.

Letu, H., Nakajima, T. Y., Ishimoto, H., Nagao, T. M., Riedi, J., Baran, A. J., Shang, H., and Kikuchi, M.: Ice cloud properties from Himawari-8/AHI next-generation geostationary satellite: Capability of the AHI to monitor the DC cloud generation process, *IEEE Trans. Geosci. Remote Sens.*, 57, 3229–3239, https://doi.org/10.1109/TGRS.2018.2882803, 2019.

Li, J., Ding, C., Li, F., and Chen, Y.: Effects of single- and double-moment microphysics schemes on the intensity of super typhoon Sarika (2016), *Atmos. Res.*, 238, 104894, https://doi.org/10.1016/j.atmosres.2020.104894, 2020.

Li, J., Geer, A. J., Okamoto, K., Otkin, J. A., Liu, Z., Han, W., and Wang, P.: Satellite all-sky infrared radiance assimilation: Recent progress and future perspectives, *Adv. Atmos. Sci.*, 39, 9–21, https://doi.org/10.1007/s00376-021-1088-9, 2022.

Line, W. E., Schmit, T. J., Lindsey, D. T., and Goodman, S. J.: Use of geostationary super rapid scan satellite imagery by the Storm Prediction Center, *Wea. Forecasting*, 31, 483–494, https://doi.org/10.1175/WAF-D-15-0135.1, 2016.

Lindsey, D., Bikos, D., and Grasso, L.: Using the GOES-16 split window difference to detect a boundary prior to cloud formation, *Bull. Amer. Meteor. Soc.*, 99, 1541–1544, https://doi.org/10.1175/BAMS-D-17-0141.1, 2018.

Lindsey, D., Schmit, T., MacKenzie, W., Jewett, C., Gunshor, M., and Grasso, L.: 10.35 µm: An atmospheric window on the GOES-R Advanced Baseline Imager with less moisture attenuation, *J. Appl. Remote Sens.*, 6, 063598, https://doi.org/10.1117/1.JRS.6.063598, 2012.

Liu, C.-Y., Chiu, C.-H., Lin, P.-H., and Min, M.: Comparison of cloud-top property retrievals from Advanced Himawari Imager, MODIS, CloudSat/CPR, CALIPSO/CALIOP, and radiosonde, *J. Geophys. Res. Atmos.*, 125, e2020JD032683, https://doi.org/10.1029/2020JD032683, 2020.

Liu, X., Griffin, A., Komurcu, M., and Huber, M.: Importance of longwave radiative forcing by icy clouds in maintaining Miocene high-latitude warmth, *Geophys. Res. Lett.*, 52, e2024GL111831, https://doi.org/10.1029/2024GL111831, 2025.

Liu, Z., Snyder, C., Guerrette, J. J., Jung, B.-J., Ban, J., Vahl, S., Wu, Y., Trémolet, Y., Auligné, T., Ménétrier, B., Shlyaeva, A., Herbener, S., Liu, E., Holdaway, D., and Johnson, B. T.: Data assimilation for the Model for Prediction Across Scales–Atmosphere with the Joint Effort for Data Assimilation Integration (JEDI–MPAS 1.0.0): EnVar implementation and evaluation, *Geosci. Model Dev.*, 15, 7859–7878, https://doi.org/10.5194/gmd-15-7859-2022, 2022.

Liu, Q., and Weng, F.: Advanced doubling-adding method for radiative transfer in planetary atmospheres, *J. Atmos. Sci.*, 63, 3459–3465, https://doi.org/10.1175/JAS3808.1, 2006.

Luo, Y., Zhang, M., Cao, Q., and Wang, L.: An evaluation of the WRF physical parameterizations for extreme rainfall simulation in the Yangtze River Middle Reaches Urban Agglomeration, *Urban Climate*, 58, 102149, https://doi.org/10.1016/j.uclim.2024.102149, 2024.

https://doi.org/10.5194/egusphere-2026-1476
Preprint. Discussion started: 18 June 2026

Mansell, E. R., Ziegler, C. L., and Bruning, E. C.: Simulated electrification of a small thunderstorm with two-moment bulk microphysics, *J. Atmos. Sci.*, 67, 171–194, https://doi.org/10.1175/2009JAS2965.1, 2010.

Matsui, T., and Coauthors: Introducing multisensor satellite radiance-based evaluation for regional Earth system modeling, *J. Geophys. Res. Atmos.*, 119, 8450–8475, https://doi.org/10.1002/2013JD021424, 2014.

Mayer, J., Mayer, B., Bugliaro, L., Meerkötter, R., and Voigt, C.: How well can brightness temperature differences of spaceborne imagers help to detect cloud phase? A sensitivity analysis regarding cloud phase and related cloud properties, *Atmos. Meas. Tech.*, 17, 5161–5185, https://doi.org/10.5194/amt-17-5161-2024, 2024.

Medeiros, B., Clement, A. C., Benedict, J. J., and Coauthors: Investigating the impact of cloud-radiative feedbacks on tropical precipitation extremes, *npj Clim. Atmos. Sci.*, 4, 18, https://doi.org/10.1038/s41612-021-00174-x, 2021.

Menzel, W. P., Frey, R. A., Baum, B. A., and Zhang, H.: MODIS cloud top properties and cloud phase algorithm theoretical basis document (Collection 6), NASA MODIS Algorithm Theoretical Basis Document, https://atmosphere-imager.gsfc.nasa.gov/sites/default/files/ModAtmo/MOD06-ATBD_2015_05_01_1.pdf, 2015.

Meyers, M. P., DeMott, P. J., and Cotton, W. R.: New primary ice-nucleation parameterizations in an explicit cloud model, *J. Appl. Meteor. Climatol.*, 31, 708–721, https://doi.org/10.1175/1520-0450(1992)031<0708:NPINPI>2.0.CO;2, 1992.

Milbrandt, J. A., and McTaggart-Cowan, R.: Sedimentation-induced errors in bulk microphysics schemes, *J. Atmos. Sci.*, 67, 3931–3948, https://doi.org/10.1175/2010JAS3541.1, 2010.

Min, M., Li, J., Wang, F., Liu, Z., and Menzel, W. P.: Retrieval of cloud top properties from advanced geostationary satellite imager measurements based on machine learning algorithms, *Remote Sensing of Environment*, 239, 111616, https://doi.org/10.1016/j.rse.2019.111616, 2020.

Mohan, P. R., Srinivas, C. V., Yesubabu, V., and Coauthors: Evaluation of WRF cloud microphysics schemes in explicit simulations of tropical cyclone 'Fani' using wind profiler radar and multi-satellite data products, *Pure Appl. Geophys.*, 181, 2317–2341, https://doi.org/10.1007/s00024-024-03517-w, 2024.

Morrison, H., Milbrandt, J. A., Bryan, G. H., Ikeda, K., Tessendorf, S. A., and Thompson, G.: Parameterization of cloud microphysics based on the prediction of bulk ice particle properties. Part II: Case study comparisons with observations and other schemes, *J. Atmos. Sci.*, 72, 312–339, https://doi.org/10.1175/JAS-D-14-0066.1, 2015.

Morrison, H., van Lier-Walqui, M., Fridlind, A. M., Grabowski, W. W., Harrington, J. Y., Hoose, C., and Xue, L.: Confronting the challenge of modeling cloud and precipitation microphysics, *J. Adv. Model. Earth Syst.*, 12, e2020MS002170, https://doi.org/10.1029/2019MS001689, 2020.

Nam, J., Cho, Y., Lim, K.-S., and Coauthors: Evaluation of four cloud microphysical schemes simulating Arctic low-level clouds observed during the ACLOUD experiment, *Asia-Pac. J. Atmos. Sci.*, 60, 727–740, https://doi.org/10.1007/s13143-024-00378-0, 2024.

Nasiri, S. L., and Kahn, B. H.: Limitations of bispectral infrared cloud phase determination and potential for improvement, *J. Appl. Meteor. Climatol.*, 47, 2895–2910, https://doi.org/10.1175/2008JAMC1879.1, 2008.

https://doi.org/10.5194/egusphere-2026-1476
Preprint. Discussion started: 18 June 2026

Neale, R., and Slingo, J.: The Maritime Continent and its role in the global climate: A GCM study, *J. Climate*, 16, 834–848, https://doi.org/10.1175/1520-0442(2003)016<0834:TMCAIR>2.0.CO;2, 2003.

Otkin, J. A., and Greenwald, T. J.: Comparison of WRF model simulated and MODIS-derived cloud data, *Mon. Weather Rev.*, 136, 1957–1970, https://doi.org/10.1175/2007MWR2293.1, 2008.

Otkin, J. A., Greenwald, T. J., Sieglaff, J., and Huang, H.-L.: Validation of a large-scale simulated brightness temperature dataset using SEVIRI satellite observations, *J. Appl. Meteor. Climatol.*, 48, 1613–1626, https://doi.org/10.1175/2009JAMC2142.1, 2009.

Otkin, J. A., Lewis, W. E., Lenzen, A. J., McNoldy, B. D., and Majumdar, S. J.: Assessing the accuracy of the cloud and water vapor fields in the Hurricane WRF (HWRF) model using satellite infrared brightness temperatures, *Mon. Weather Rev.*, 145, 2027–2046, https://doi.org/10.1175/MWR-D-16-0354.1, 2017.

Painemal, D., Minnis, P., and O'Neill, L.: The diurnal cycle of cloud-top height and cloud cover over the southeastern Pacific as observed by GOES-10, *J. Atmos. Sci.*, 70, 2393–2408, https://doi.org/10.1175/JAS-D-12-0325.1, 2013.

Panegrossi, G., and Coauthors: Use of the GPM constellation for monitoring heavy precipitation events over the Mediterranean region, *IEEE Journal of Selected Topics in Applied Earth Observations and Remote Sensing*, 9, 2733–2753, https://doi.org/10.1109/JSTARS.2016.2520660, 2016.

Pandey, A., Lamraoui, F., Smith, J. B., Clapp, C. E., Sayres, D. S., and Kuang, Z.: Sensitivity of deep convection and cross-tropopause water transport to microphysical parameterizations in WRF, *J. Geophys. Res. Atmos.*, 128, e2022JD037053, https://doi.org/10.1029/2022JD037053, 2023.

Park, S., Lee, D.-K., and Lee, J.: Impact of microphysics schemes on the simulation of a tropical cyclone observed during TCS-08, *J. Geophys. Res. Atmos.*, 124, 7421–7442, https://doi.org/10.1029/2019JD032288, 2019.

Pavolonis, M., and Calvert, C.: NOAA Enterprise cloud type and cloud phase, version 3, Algorithm Theoretical Basis Document, *NOAA NESDIS Center for Satellite Applications and Research*, 106 pp., https://www.star.nesdis.noaa.gov/goesr/documents/ATBDs/Enterprise/ATBD_Enterprise_Cloud_Type_v3_2020-06-01.pdf, 2020.

Pavolonis, M. J., Heidinger, A. K., and Uttal, T.: GOES-R Advanced Baseline Imager (ABI) algorithm theoretical basis document for cloud type and cloud phase, version 2.0, *NOAA NESDIS Center for Satellite Applications and Research*, 86 pp., https://www.star.nesdis.noaa.gov/goesr/docs/ATBD/Cloud_Phase.pdf, 2010.

Pepin, N. C., Arnone, E., Gobiet, A., Haslinger, K., Kotlarski, S., Notarnicola, C., et al.: Climate changes and their elevational patterns in the mountains of the world, *Rev. Geophys.*, 60, e2020RG000730, https://doi.org/10.1029/2020RG000730, 2022.

Rendon, J., and Zhang, Y.: Impact of microphysical parameterizations on satellite all-sky infrared data assimilation and practical predictability of Hurricane Harvey (2017), *J. Geophys. Res. Atmos.*, 130, e2024JD042697, https://doi.org/10.1029/2024JD042697, 2025.

Schmit, T. J., Griffith, P., Gunshor, M. M., Daniels, J. M., Goodman, S. J., and Lebair, W. J.: A closer look at the ABI on the GOES-R series, *Bull. Amer. Meteor. Soc.*, 98, 681–698, https://doi.org/10.1175/BAMS-D-15-00230.1, 2017.

https://doi.org/10.5194/egusphere-2026-1476
Preprint. Discussion started: 18 June 2026

Serra, Y. L., Rutledge, S. A., Chudler, K., and Zhang, C.: Rainfall and convection in ERA5 and MERRA-2 over the northern equatorial western Pacific during PISTON, *J. Climate*, 36, 845–863, https://doi.org/10.1175/JCLI-D-22-0203.1, 2023.

Sieron, S. B., Clothiaux, E. E., Zhang, F., Lu, Y., and Otkin, J. A.: Comparison of using distribution-specific versus effective radius methods for hydrometeor single-scattering properties for all-sky microwave satellite radiance simulations with different microphysics parameterization schemes, *J. Geophys. Res. Atmos.*, 122, 7027–7046, https://doi.org/10.1002/2017JD026494, 2017.

Simón-Moral, A., Dipankar, A., Doan, Q.-V., Sanchez, C., Roth, M., Becker, E., and Coauthors: Urban intensification of convective rainfall over the Singapore–Johor Bahru region, *Q. J. R. Meteorol. Soc.*, 147, 3665–3680, https://doi.org/10.1002/qj.4147, 2021.

Skamarock, W. C., Klemp, J. B., Duda, M. G., Fowler, L. D., Park, S.-H., and Ringler, T. D.: A multiscale nonhydrostatic atmospheric model using centroidal Voronoi tessellations and C-grid staggering, *Mon. Weather Rev.*, 140, 3090–3105, https://doi.org/10.1175/MWR-D-11-00215.1, 2012.

Skamarock, W. C., Duda, M. G., Ha, S., and Park, S.-H.: Limited-area atmospheric modeling using an unstructured mesh, *Mon. Weather Rev.*, 146, 3445–3460, https://doi.org/10.1175/MWR-D-18-0155.1, 2018.

Sokol, A. B., and Hartmann, D. L.: Tropical anvil clouds: Radiative driving toward a preferred state, *J. Geophys. Res. Atmos.*, 125, e2020JD033107, https://doi.org/10.1029/2020JD033107, 2020.

Stephens, G. L., Shiro, K. A., Hakuba, M. Z., and Coauthors: Tropical deep convection, cloud feedbacks and climate sensitivity, *Surv. Geophys.*, 45, 1903–1931, https://doi.org/10.1007/s10712-024-09831-1, 2024.

Sunny Lim, K., Chang, E., Sun, R., Kim, K., Tapiador, F. J., and Lee, G.: Evaluation of simulated winter precipitation using WRF-ARW during the ICE-POP 2018 field campaign, *Wea. Forecasting*, 35, 2199–2213, https://doi.org/10.1175/WAF-D-19-0236.1, 2020.

Susskind, J., Blaisdell, J. M., Iredell, L., and Keita, F.: Improved temperature sounding and quality control methodology using AIRS/AMSU data: The AIRS Science Team Version 5 retrieval algorithm, *IEEE Trans. Geosci. Remote Sens.*, 49, 883–907, https://doi.org/10.1109/TGRS.2010.2070508, 2011.

Thompson, M., Tewari, K., Ikeda, K., Tessendorf, S., Weeks, C., Otkin, J. A., and Kong, F.: Explicitly coupled cloud physics and radiation parameterizations and subsequent evaluation in WRF high-resolution convective forecasts, *Atmos. Res.*, 168, 92–104, https://doi.org/10.1016/j.atmosres.2015.09.005, 2016.

Tong, M., and Xue, M.: Simultaneous estimation of microphysical parameters and atmospheric state with radar data and ensemble square-root Kalman filter. Part I: Sensitivity analysis and parameter identifiability, *Mon. Weather Rev.*, 136, 1630–1648, https://doi.org/10.1175/2007MWR2070.1, 2008.

Trémolet, Y., and Auligné, T.: The Joint Effort for Data Assimilation Integration (JEDI), *JCSDA Quarterly Newsletter*, 66, 1–5, https://doi.org/10.25923/RB19-0Q26, 2020.

https://doi.org/10.5194/egusphere-2026-1476
Preprint. Discussion started: 18 June 2026

Van Weverberg, K., and Coauthors: Comparison of one-moment and two-moment bulk microphysics for high-resolution climate simulations of intense precipitation, *Atmos. Res.*, 147, 145–161, https://doi.org/10.1016/j.atmosres.2014.05.012, 2014.

Van Weverberg, K., Vogelmann, A. M., Lin, W., and Coauthors: The role of cloud microphysics parameterization in the simulation of mesoscale convective system clouds and precipitation in the tropical western Pacific, *J. Atmos. Sci.*, 70, 1104–1128, https://doi.org/10.1175/JAS-D-12-0104.1, 2013.

Waliser, D. E., Li, J. L. F., Woods, C. P., and Coauthors: Cloud ice: A climate model challenge with signs and expectations of progress, *J. Geophys. Res. Atmos.*, 114, D08209, https://doi.org/10.1029/2008JD010015, 2009.

Wall, C. J., Hartmann, D. L., Thieman, M. M., Smith, W. L., and Minnis, P.: The life cycle of anvil clouds and the top-of-atmosphere radiation balance over the tropical west Pacific, *J. Climate*, 31, 10059–10080, https://doi.org/10.1175/JCLI-D-18-0154.1, 2018.

Wang, C., Yang, P., Platnick, S., Heidinger, A. K., Baum, B. A., Greenwald, T., Zhang, Z., and Holz, R. E.: Retrieval of ice cloud properties from AIRS and MODIS observations based on a fast high-spectral-resolution radiative transfer model, *J. Appl. Meteor. Climatol.*, 52, 710–726, https://doi.org/10.1175/JAMC-D-12-020.1, 2013.

Wang, X., Chipilski, H. G., Bishop, C. H., Satterfield, E., Baker, N., and Whittaker, J.: A multiscale local gain form ensemble transform Kalman filter (MLGETKF), *Mon. Weather Rev.*, 149, 605–622, https://doi.org/10.1175/MWR-D-20-0290.1, 2021.

Wang, Y., Su, H., Jiang, J. H., Xu, F., and Yung, Y. L.: Impact of cloud ice particle size uncertainty in a climate model and implications for future satellite missions, *J. Geophys. Res. Atmos.*, 125, e2019JD032119, https://doi.org/10.1029/2019JD032119, 2020.

Wang, Y., and Zhao, C.: Can MODIS cloud fraction fully represent the diurnal and seasonal variations at DOE ARM SGP and Manus sites? *J. Geophys. Res. Atmos.*, 122, 329–343, https://doi.org/10.1002/2016JD025954, 2017.

Wang, Y., Liu, Z., Yang, S., Min, J., Chen, L., Chen, Y., and Zhang, T.: Added value of assimilating Himawari-8 AHI water vapor radiances on analyses and forecasts for the “7.19” severe storm over North China, *J. Geophys. Res. Atmos.*, 123, 3374–3394, https://doi.org/10.1002/2017JD027697, 2018.

Wang, T., Zhu, J., Lei, H., Shi, Y., Guo, J., and Gao, Z.: Comparison of microphysics parameterization schemes on cloud macrophysics forecasts for mixed convective–stratiform cloud events, *Atmos. Res.*, 277, 106284, https://doi.org/10.1016/j.atmosres.2022.106284, 2022.

Wang, T., Zhu, J., Lei, H., Shi, Y., Guo, J., and Gao, Z.: Comparison of microphysics parameterization schemes on cloud macrophysics forecasts for mixed convective-stratiform cloud events, *Atmos. Res.*, 277, 106284, https://doi.org/10.1016/j.atmosres.2022.106284, 2022.

Wei, Y., and Pu, Z.: Diurnal cycle of precipitation and near-surface atmospheric conditions over the Maritime Continent: Land–sea contrast and impacts of ambient winds in cloud-permitting simulations, *Clim. Dyn.*, 58, 2421–2449, https://doi.org/10.1007/s00382-021-06012-3, 2022

https://doi.org/10.5194/egusphere-2026-1476
Preprint. Discussion started: 18 June 2026

Wheatley, D. M., Yussouf, N., and Stensrud, D. J.: Ensemble Kalman filter analyses and forecasts of a severe mesoscale convective system using different choices of microphysics schemes, *Mon. Weather Rev.*, 142, 3243–3263, https://doi.org/10.1175/MWR-D-13-00260.1, 2014.

Xu, K.-M., and Randall, D. A.: A semiempirical cloudiness parameterization for use in climate models, *J. Atmos. Sci.*, 53, 3084–3102, https://doi.org/10.1175/1520-0469(1996)053<3084:ASCPFU>2.0.CO;2, 1996.

Yao, B., Liu, C., Yin, Y., Zhang, P., Min, M., and Han, W.: Radiance-based evaluation of WRF cloud properties over East Asia: Direct comparison with FY-2E observations, *J. Geophys. Res. Atmos.*, 123, 4613–4629, https://doi.org/10.1029/2017JD027600, 2018.

Yang, K., et al.: On downward shortwave and longwave radiations over high-altitude regions: observations and modeling in the Tibetan Plateau, *Atmos. Res.*, 150, 38–51, https://doi.org/10.1016/j.atmosres.2014.01.016, 2010.

Zhang, X., Jiang, L., Liu, Z., Sun, T., Wang, W., and Chen, I.-H.: Assessing Cloud Representation in Two Microphysics Schemes of MPAS-Atmosphere Model (version 8.2.2) with Himawari-9 AHI Observations, Zenodo [code], https://doi.org/10.5281/zenodo.19925596, 2026a.

Zhang, X., Liu, Z., Sun, T., and Chen, I.-H.: Processed Observation Datasets for "Assessing Cloud Representation in Two Microphysics Schemes of the MPAS-Atmosphere Model (Version 8.2.2) Using Himawari-9 AHI Observations", Zenodo [data set], https://doi.org/10.5281/zenodo.20312122, 2026b.

Zhang, Y., Fan, J., Li, Z., and Rosenfeld, D.: Impacts of cloud microphysics parameterizations on simulated aerosol–cloud interactions for deep convective clouds over Houston, *Atmos. Chem. Phys.*, 21, 2363–2381, https://doi.org/10.5194/acp-21-2363-2021, 2021.

Zhang, Y., Wang, Y., Liu, G., and Guo, J.: Satellite-based assessment of various cloud microphysics schemes in simulating typhoon hydrometeors, *Adv. Meteorol.*, 2019, 3168478, https://doi.org/10.1155/2019/3168478, 2019.

Zhu, K., Xue, M., Yang, N., and Zhang, C.: How well does 4-km WRF model predict three-dimensional reflectivity structure over China as compared to radar observations?, *J. Geophys. Res. Atmos.*, 128, e2022JD038143, doi:10.1029/2022JD038143, 2023.

Zhu, Z., Gu, J., Xu, B., and Shi, C.: Characterization of Himawari-8/AHI to Himawari-9/AHI infrared observations continuity, *Int. J. Remote Sens.*, 45, 121–142, https://doi.org/10.1080/01431161.2023.2293476, 2023.